

Holographic MIMO Communications

Andrea Pizzo, *Member, IEEE*, Luca Sanguinetti, *Senior Member, IEEE*,

Thomas L. Marzetta, *Life Fellow, IEEE*

Abstract

Imagine a MIMO communication system that fully exploits the propagation characteristics offered by an electromagnetic channel and ultimately approaches the limits imposed by wireless communications. This is the concept of Holographic MIMO communications. Accurate and tractable channel modeling is critical to understanding its full potential. Classical stochastic models used by communications theorists are derived under the electromagnetic far-field assumption. However, such assumption breaks down when large (compared to the wavelength) antenna arrays are considered - as envisioned in future wireless communications. In this paper, we start from the first principles of wave propagation and provide a Fourier plane-wave series expansion of the channel response, which fully captures the essence of electromagnetic propagation in arbitrary scattering and is also valid in the (radiative) near-field. The expansion is based on the Fourier spectral representation and has an intuitive physical interpretation, as it statistically describes the angular coupling between source and receiver. When discretized, it leads to a low-rank semi-unitarily equivalent approximation of the spatial electromagnetic channel in the angular domain. The developed channel model is used to compute the ergodic capacity of a Holographic MIMO system with different degrees of channel state information.

Index Terms

Electromagnetic MIMO channel modeling, near-field communications, plane-wave decomposition, Fourier spectral representation, Holographic MIMO.

I. INTRODUCTION

Communication theorists are constantly looking for new technologies to increase the information rate and reliability of wireless communications. Chief among the technologies that blossomed into major advances is the multiple antenna technology, whose latest instantiation, i.e., Massive MIMO (multiple-input multiple-output), became a reality in 5G. It is thus time for the research community to look for new multiple antenna technologies to meet the higher data rate, reliability, and traffic demands in the beyond 5G era. Inspired by the potential benefits of Massive MIMO with more and more antennas, most of the new research directions envision the use of dense

Part of this work was presented at the Asilomar Conference on signals, Systems and Computers, Pacific Grove, CA, 2021 [1]. A. Pizzo and L. Sanguinetti are with the Dipartimento di Ingegneria dell'Informazione, University of Pisa, 56122 Pisa, Italy (andrea.pizzo@ing.unipi.it, luca.sanguinetti@unipi.it). T. Marzetta is with the Department of Electrical and Computer Engineering, Tandon School of Engineering, 11201 Brooklyn, NY (tom.marzetta@nyu.edu).

TABLE I. Electromagnetic propagation regimes for different MIMO apertures.

Maximum size L [m]	R [m] @ 3 GHz	R [m] @ 28 GHz	R [m] @ 73 GHz	R [m] @ 142 GHz
0.1	—	1.9	4.9	9
0.5	5	47	122	237
1	20	187	487	—
3	180	—	—	—

antenna arrays with large size (compared to the wavelength λ), and are taking place under different names, e.g., Holographic MIMO [1]–[4], large intelligent surfaces [5], [6], and reconfigurable intelligent surfaces [7], [8]. When an antenna array much larger than the wavelength is used, a fundamental phenomenon appears: the electromagnetic propagation regime is pushed from the Fraunhofer far-field region (i.e., the receiver is at a distance $R > 2L^2/\lambda$ from the array with maximum size L) towards the Fresnel near-field region (i.e., with $R \leq 2L^2/\lambda$) [4]. Table I reports the Fraunhofer distance in meters for planar arrays of practical size at 3, 28, 73, and 142 GHz carrier frequencies [9]. As seen, the near-field operating regime may occur at any frequency if specific (e.g., not only short- but also mid-range) applications are considered.

From the above discussion, it thus follows that the realistic design and performance assessment of large antenna technologies requires accurate and tractable channel models that are valid also in near-field. Deterministic models (e.g., based on ray-tracing) achieve the highest accuracy as they provide accurate predictions of signal propagation in a given environment [10]. However, they rely on numerical electromagnetic solvers of the Maxwell's equations, and hence, they are too site-specific [10]. Stochastic models are the most desirable for communication theorists to work with since they permit to draw general theoretical inferences [11]. Physically meaningful stochastic models are based on the channel expansion in terms of plane-waves, as they provide a natural eigensolution of the Helmholtz equation [12]. Plane-wave based models allow also to decouple scattering conditions from array characteristics [13]. However, plane-wave based models are typically used in wireless research only under the assumption that source and receiver are at a very large distance such that wavefronts can be approximated as locally planar over the entire arrays [13]–[19]. An example is given by the virtual channel representation pioneered in [14], [15]. Recently, [20], [21] have brought to the attention of wireless community that wave propagation can be generally formulated in terms of plane-waves irrespective of the distance between source and receiver (i.e., even in the near-field) and under arbitrary scattering conditions. This paper leverages this result to provide the following contributions.

A. Contributions

We consider wireless communications between two parallel planar arrays in a three-dimensional (3D) scattered medium and provide an approximated Fourier plane-wave series expansion of the electromagnetic channel, which may be regarded as the asymptotic Karhunen-Loeve expansion of a spatially-stationary random electromagnetic channel when $L/\lambda \gg 1$. It is based on the Fourier spectral representation of a random process (e.g., [22]), which yields asymptotically uncorrelated complex-Gaussian random coefficients whose statistics are completely determined by their variances. These have an intuitive physical interpretation as being the strengths of the angular coupling between the source and receive arrays and can thus be measured accordingly. They are determined by the joint propagation characteristics at both ends. Physically, the provided model finds its applicability even in the near-field region, as it does not rely on the electromagnetic far-field assumption, but is rather built upon the physics fundamentals of wave propagation [21].

Suitably discretized under Nyquist's condition, the Fourier plane-wave series expansion yields a stochastic description of the electromagnetic MIMO channel in which the array geometry and scattering conditions are perfectly separated. The former is a deterministic effect that changes the domain of representation from spatial to angular domains (and vice-versa) and is performed by a double two-dimensional (2D) discrete spatial Fourier transform. The latter is a stochastic effect that accounts for wave propagation. Notably, the angular domain provides a low-rank semi-unitarily equivalent approximation of the spatial electromagnetic channel. The decoupling property of the model yields an efficient hybrid structure for the transceiver architecture that accounts for a double 2D discrete Fourier transform (DFT) operation in the analog stage and enables the design of array configuration and signal processing algorithms separately. Since the spatial domain offers a highly redundant description of the electromagnetic channel, a significant complexity reduction (e.g., channel estimation, optimal signaling, coding) can be achieved. The developed channel model is finally used to compute the ergodic capacity for different degrees of channel state information.

B. Outline of the Paper and Notation

The remainder of this paper is organized as follows. In Section II, we briefly review the Fourier plane-wave integral representation from [21]. This is used in Section III to derive a novel Fourier plane-wave series expansion of the electromagnetic channel. Suitably discretized, this expansion yields in Section IV a stochastic description of an electromagnetic MIMO channel. Section V uses

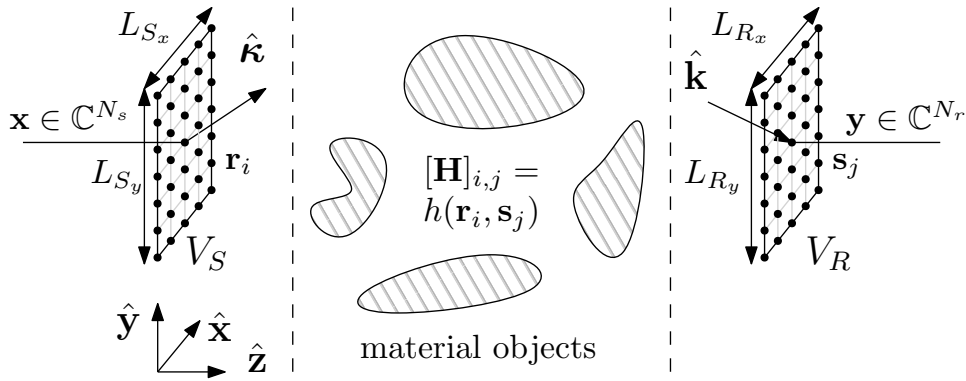


Fig. 1. MIMO communications system under arbitrary scattering.

the provided model to analyze the capacity of the channel in the angular domain and includes numerical results for illustration. Final discussions are drawn in Section VI.

We use upper (lower) case letters for angular (spatial) entities. Boldfaced letters are used for vectors and matrices. Sets are indicated by calligraphic letters, and have Lebesgue measure $|\mathcal{X}|$. $\mathbb{1}_{\mathcal{X}}(x)$ is the indicator function and $\mathbb{E}\{\cdot\}$ denotes the expectation operator. The notation $n \sim \mathcal{N}_{\mathbb{C}}(0, \sigma^2)$ stands for a circularly-symmetric complex-Gaussian random variable with variance σ^2 . The superscripts ^T and ^H stand for transposition and hermitian transposition. The Hadamard and Kronecker products are $\mathbf{A} \odot \mathbf{B}$ and $\mathbf{A} \otimes \mathbf{B}$, respectively. \mathbf{I}_N is the $N \times N$ identity matrix and $\mathbf{0}_N$ is the N -dimensional zero vector. We denote $\text{diag}(\mathbf{a})$ the diagonal matrix with elements from \mathbf{a} . \mathbb{R}^n is the n -dimensional real-valued Euclidean space. A general point in \mathbb{R}^3 is described by $\mathbf{r} = x\hat{\mathbf{x}} + y\hat{\mathbf{y}} + z\hat{\mathbf{z}}$ where $\hat{\mathbf{x}}$, $\hat{\mathbf{y}}$, and $\hat{\mathbf{z}}$ are three orthonormal vectors, and (x, y, z) are its Cartesian coordinates. The length of \mathbf{r} is $\|\mathbf{r}\| = \sqrt{x^2 + y^2 + z^2}$ and $\hat{\mathbf{r}} = \mathbf{r}/\|\mathbf{r}\|$ is the unit vector.

II. PRELIMINARIES

Consider the two parallel and $\hat{\mathbf{z}}$ -oriented planar arrays¹ depicted in Fig. 1, which span the rectangular regions $V_S \subset \mathbb{R}^3$ and $V_R \subset \mathbb{R}^3$ of xy -dimensions $L_{S,x}$, $L_{S,y}$ and $L_{R,x}$, $L_{R,y}$, respectively. The transmit array is equipped with N_s antenna elements while the receive array has N_r antennas. Wave propagation takes place in the form of monochromatic scalar waves (i.e., with no polarization), at radiation frequency ω (corresponding to a wavelength λ), in a 3D scattered, homogeneous, and infinite medium. We assume that there is no direct path due to the presence of material objects, which are homogeneous and made up of arbitrary shape and size.

¹Volumetric arrays do not offer extra degrees of freedom over planar arrays [2], [21].

A. MIMO communications

At any arbitrary symbol time, the MIMO system in Fig. 1 is described by the following discrete-space input-output relation(e.g., [23]):

$$\mathbf{y} = \mathbf{H}\mathbf{x} + \mathbf{n} \quad (1)$$

where $\mathbf{y} \in \mathbb{C}^{N_r}$ and $\mathbf{x} \in \mathbb{C}^{N_s}$ denote the received and transmitted signal vectors, respectively. Also, $\mathbf{n} \in \mathbb{C}^{N_r}$ accounts for thermal noise that is distributed as $\mathbf{n} \sim \mathcal{N}_{\mathbb{C}}(\mathbf{0}, \sigma^2 \mathbf{I}_{N_r})$. Here, the entry $[\mathbf{H}]_{ij}$ represents the propagation coefficient between the j th transmitting antenna located at point \mathbf{s}_j and the i th receiving antenna located at point \mathbf{r}_i . In wireless communications, the entries $[\mathbf{H}]_{ij}$ are typically modeled as a stationary sequence of circularly-symmetric, complex-Gaussian and correlated random variables. As a consequence, \mathbf{H} is a correlated Rayleigh fading channel matrix that is uniquely described by its spatial correlation matrix

$$\mathbf{R} = \mathbb{E}\{\text{vec}(\mathbf{H})\text{vec}(\mathbf{H})^H\} \quad (2)$$

The classical approach is to develop physically-meaningful models for \mathbf{R} from which realizations of \mathbf{H} are then obtained. Unlike the classical approach, this paper builds upon the statistical model developed in [3], [21] that, starting from first electromagnetic principles of wave propagation, provides us with a four-dimensional (4D) Fourier plane-wave representation of $h(\mathbf{r}, \mathbf{s})$. Here, $h(\mathbf{r}, \mathbf{s})$ denotes the random channel response at point \mathbf{r} due to a unit impulse (point source) applied at point \mathbf{s} . The MIMO channel is obtained by sampling $h(\mathbf{r}, \mathbf{s})$ at $\mathbf{s}_j = [s_{x_j}, s_{y_j}, s_z]^T$ and $\mathbf{r}_i = [r_{x_i}, r_{y_i}, r_z]^T$ for $j = 1, \dots, N_s$ and $i = 1, \dots, N_r$, and for any fixed pair of s_z and r_z with $r_z > s_z$, as

$$[\mathbf{H}]_{ij} = h(\mathbf{r}_i, \mathbf{s}_j). \quad (3)$$

Notice that the plane-wave representation of $h(\mathbf{r}, \mathbf{s})$ is asymptotically exact as $\min(L_{S,x}, L_{S,y})/\lambda \rightarrow \infty$ and $\min(L_{R,x}, L_{R,y})/\lambda \rightarrow \infty$ jointly [21]. The key results from [3], [21] are reviewed next as they are instrumental for Section III where a Fourier plane-wave series expansion is derived that well approximates $h(\mathbf{r}, \mathbf{s})$ when $\min(L_{S,x}, L_{S,y})/\lambda \gg 1$ and $\min(L_{R,x}, L_{R,y})/\lambda \gg 1$ jointly.

Remark 1. *The wireless channel is composed of large-scale fading and small-scale fading. The former occurs on a larger scale — a few hundred wavelengths — and is due to pathloss, shadowing, and antenna gains, while the latter is a microscopic effect caused by small variations in the propagation. If the array size at both ends does not exceed the size of the local scattering neighborhood, the two components can be modelled independently (e.g., [24, Sec. 3.6]). This paper only considers the small-scale fading. Any large-scale fading model can be applied verbatim.*

B. Fourier plane-wave representation of electromagnetic channels

Once the reactive propagation mechanisms taking place in the proximity of source and material objects (i.e., at a distance of few wavelengths) are excluded, the channel response $h(\mathbf{r}, \mathbf{s})$ can be modeled as a *spatially-stationary* electromagnetic random field [21, Sec. IV.A]. For this general class of channels, we can always find an *exact* statistical representation of $h(\mathbf{r}, \mathbf{s})$ in terms of plane-waves that is given by the Fourier plane-wave representation in (4); see [21, Sec. IV] for more details. In particular, $h(\mathbf{r}, \mathbf{s})$ can be represented as

$$h(\mathbf{r}, \mathbf{s}) = \frac{1}{(2\pi)^2} \iiint_{\mathcal{D} \times \mathcal{D}} a_r(\mathbf{k}, \mathbf{r}) H_a(k_x, k_y, \kappa_x, \kappa_y) a_s(\boldsymbol{\kappa}, \mathbf{s}) dk_x dk_y d\kappa_x d\kappa_y \quad (4)$$

and it is thus decomposed into three terms. The first term $a_s(\boldsymbol{\kappa}, \mathbf{s})$ is the *source response* that maps the impulsive excitation current at point \mathbf{s} to the source propagation direction $\hat{\boldsymbol{\kappa}} = \boldsymbol{\kappa}/\|\boldsymbol{\kappa}\|$ of the incident field. The second term $a_r(\mathbf{k}, \mathbf{r})$ is the *receive response* that maps the receive propagation direction $\hat{\mathbf{k}} = \mathbf{k}/\|\mathbf{k}\|$ of the receive field to the induced current at point \mathbf{r} . They are defined as

$$a_s(\boldsymbol{\kappa}, \mathbf{s}) = e^{-j\boldsymbol{\kappa}^T \mathbf{s}} = e^{-j(\kappa_x s_x + \kappa_y s_y + \gamma(\kappa_x, \kappa_y) s_z)} \quad (5)$$

$$a_r(\mathbf{k}, \mathbf{r}) = e^{j\mathbf{k}^T \mathbf{r}} = e^{j(k_x r_x + k_y r_y + \gamma(k_x, k_y) r_z)} \quad (6)$$

where $\boldsymbol{\kappa} = \kappa_x \hat{\mathbf{x}} + \kappa_y \hat{\mathbf{y}} + \gamma(\kappa_x, \kappa_y) \hat{\mathbf{z}}$ and $\mathbf{k} = k_x \hat{\mathbf{x}} + k_y \hat{\mathbf{y}} + \gamma(k_x, k_y) \hat{\mathbf{z}}$ are the corresponding wave vectors, and $\gamma(\cdot, \cdot)$ is defined as

$$\gamma(k_x, k_y) = \sqrt{\kappa^2 - k_x^2 - k_y^2} \quad (7)$$

with $\kappa = 2\pi/\lambda$. The integration region in (4) is limited to the support

$$\mathcal{D} = \{(k_x, k_y) \in \mathbb{R}^2 : k_x^2 + k_y^2 \leq \kappa^2\} \quad (8)$$

given by a centered disk of radius κ . As a result, $\gamma(\cdot, \cdot)$ is always real-valued and the representation in (4) involves propagating plane-waves only. Note that this is due to the spatial stationarity of $h(\mathbf{r}, \mathbf{s})$ that reveals the low-pass filter behavior of the electromagnetic channel. The third term $H_a(k_x, k_y, \kappa_x, \kappa_y)$ in (4) is the *angular response* that maps every incident direction $\hat{\boldsymbol{\kappa}}$ onto every receive direction $\hat{\mathbf{k}}$. Its statistical structure is given in the following theorem.

Theorem 1. [21, Th. 2] *If $h(\mathbf{r}, \mathbf{s})$ is a spatially-stationary, circularly-symmetric and complex-Gaussian random field, the angular response $H_a(k_x, k_y, \kappa_x, \kappa_y)$ is of the form*

$$H_a(k_x, k_y, \kappa_x, \kappa_y) = \frac{\kappa\eta}{2} \frac{A(k_x, k_y, \kappa_x, \kappa_y) W(k_x, k_y, \kappa_x, \kappa_y)}{\gamma^{1/2}(k_x, k_y) \gamma^{1/2}(\kappa_x, \kappa_y)} \quad (9)$$

where $A(k_x, k_y, \kappa_x, \kappa_y)$ is an arbitrary real-valued, non-negative function (called spectral factor) and $W(k_x, k_y, \kappa_x, \kappa_y)$ is a collection of unit-variance, independent and identically distributed (i.i.d.) circularly-symmetric and complex-Gaussian random variables, i.e., $W(k_x, k_y, \kappa_x, \kappa_y) \sim \mathcal{N}_{\mathbb{C}}(0, 1)$.

Plugging (9) into (4) generates a stationary random field that converges in the mean-squared sense to the actual channel field $h(\mathbf{r}, \mathbf{s})$ for any practical channel with bounded spectral factor $A(k_x, k_y, \kappa_x, \kappa_y)$ [21, Lemma 2]. It provides a second-order characterization of the channel response in terms of statistically independent Gaussian random coefficients. In fact, (4) is directly connected to the Fourier spectral representation of a spatial random field; see [21, Sec. IV] for more details.

Remark 2. A key property of (4) is the decoupling of array geometry and scattering. While the former is a deterministic effect represented by the source and receive responses, the latter is stochastic and entirely embedded into the angular response in (9). In Section IV, this property will lead to a MIMO channel model whose spatial correlation matrix has a decoupled structure, thereby enabling the design of array configurations and signal processing algorithms separately.

C. Physical considerations

The angular response $H_a(k_x, k_y, \kappa_x, \kappa_y)$ describes the channel coupling between every pair of source $\hat{\kappa}$ and receive $\hat{\mathbf{k}}$ propagation directions. We may rewrite (9) as

$$H_a(k_x, k_y, \kappa_x, \kappa_y) = S^{1/2}(k_x, k_y, \kappa_x, \kappa_y) W(k_x, k_y, \kappa_x, \kappa_y) \quad (10)$$

where $S(k_x, k_y, \kappa_x, \kappa_y)$ is a non-negative function defined as²

$$S(k_x, k_y, \kappa_x, \kappa_y) = \frac{A^2(k_x, k_y, \kappa_x, \kappa_y)}{\gamma(k_x, k_y) \gamma(\kappa_x, \kappa_y)}. \quad (11)$$

Plugging (10) into (4) the average channel power $P_h = \mathbb{E}\{|h(\mathbf{r}, \mathbf{s})|^2\} < \infty$ is [21, Eq. (62)]:

$$P_h = \frac{1}{(2\pi)^4} \iiint_{-\infty}^{\infty} S(k_x, k_y, \kappa_x, \kappa_y) d\kappa_x d\kappa_y dk_x dk_y \quad (12)$$

where $S(k_x, k_y, \kappa_x, \kappa_y)$ represents the *bandlimited* 4D power spectral density of $h(\mathbf{r}, \mathbf{s})$. If $h(\mathbf{r}, \mathbf{s})$ is assumed to have unit average power, then $S(k_x, k_y, \kappa_x, \kappa_y)$ can be regarded as the *continuous angular power distribution* of the channel, which specifies how the power is distributed angularly between every pair of source $\hat{\kappa}$ and receive $\hat{\mathbf{k}}$ propagation directions, on average. From (11), it follows that it is fully described by the spectral factor $A(k_x, k_y, \kappa_x, \kappa_y)$ that physically accounts for

²Unlike [21, Eq. (56)], in (11) the coefficient $(\kappa\eta/2)^2$ is embedded into the spectral factor $A(k_x, k_y, \kappa_x, \kappa_y)$.

the angular selectivity of the scattering. Notice that an isotropic scattering condition is described by a constant spectral factor, i.e., $A(k_x, k_y, \kappa_x, \kappa_y) = A(\kappa)$, as the transfer of power is uniformly distributed over all propagation directions [3], [21]. Under non-isotropic scattering conditions, $A(k_x, k_y, \kappa_x, \kappa_y)$ can varies arbitrarily and thus the bandwidth of $h(\mathbf{r}, \mathbf{s})$ is determined by the support of $S(k_x, k_y, \kappa_x, \kappa_y)$ in (11), as summarized next.

Corollary 1. [21] $h(\mathbf{r}, \mathbf{s})$ is circularly-bandlimited with maximum bandwidth $|\mathcal{D}| = \pi\kappa^2$, which is achieved under isotropic scattering conditions.

As derived in [3, Lemma 2], under isotropic propagation conditions the correlation function between two antennas at a distance r yields the well-known Clarke's isotropic $\text{sinc}(2r/\lambda)$ correlation. This shows that (4) embraces existing models and proves its asymptotic validity since the Clarke's model is exact under isotropic propagation [3].

III. FOURIER PLANE-WAVE SERIES OF STOCHASTIC ELECTROMAGNETIC CHANNELS

For any fixed pair of s_z and r_z , the incident and received plane-waves in (5) and (6) correspond to two phase-shifted versions of 2D spatial-frequency Fourier harmonics. Intuitively, the transition from the Fourier plane-wave spectral representation to a Fourier plane-wave series expansion is analogous to the Fourier integral-Fourier series transition for time-domain signals. This is the main result of this section, which is summarized in Theorem 2 below and provides us with an approximation of the Fourier plane-wave representation in (4). The approximation is accurate in the large array regime, as summarized in the following assumption.

Assumption 1. Planar arrays are such that $\min(L_{S,x}, L_{S,y})/\lambda \gg 1$ and $\min(L_{R,x}, L_{R,y})/\lambda \gg 1$.

The above assumption does not require the arrays to be “physically large”, but rather their normalized size (with respect to the wavelength λ). This is analogous to the Nyquist-Shannon sampling theorem for bandlimited waveform channels $h(t)$ of bandwidth B , observed over time interval $[0, T]$ (e.g., [25]). For this class of channels, we can approximate $h(t)$ as a linear combination of a finite number of cardinal basis functions with coefficients collected inside $[0, T]$ and equally spaced by $1/2B$. The approximation error within $[0, T]$ becomes negligible as $BT \rightarrow \infty$.

A. Main result

With a slight abuse of notation, we call

$$a_s(m_x, m_y, \mathbf{s}) = e^{-j\left(\frac{2\pi}{L_{S,x}}m_x s_x + \frac{2\pi}{L_{S,y}}m_y s_y + \gamma_s(m_x, m_y)s_z\right)} \quad (13)$$

$$a_r(\ell_x, \ell_y, \mathbf{r}) = e^{j\left(\frac{2\pi}{L_{R,x}}\ell_x r_x + \frac{2\pi}{L_{R,y}}\ell_y r_y + \gamma_r(\ell_x, \ell_y)r_z\right)} \quad (14)$$

the discretized plane-waves obtained by evaluating (κ_x, κ_y) at $(2\pi m_x/L_{S,x}, 2\pi m_y/L_{S,y})$ and (k_x, k_y) at $(2\pi \ell_x/L_{R,x}, 2\pi \ell_y/L_{R,y})$, respectively. Consequently, we have that

$$\gamma_s(m_x, m_y) = \gamma\left(\frac{2\pi}{L_{S,x}}m_x, \frac{2\pi}{L_{S,y}}m_y\right) \quad \text{and} \quad \gamma_r(\ell_x, \ell_y) = \gamma\left(\frac{2\pi}{L_{R,x}}\ell_x, \frac{2\pi}{L_{R,y}}\ell_y\right) \quad (15)$$

where $\gamma(\cdot, \cdot)$ is given by (7). Since the angular response $H_a(k_x, k_y, \kappa_x, \kappa_y)$ is non-zero only within the support $(k_x, k_y, \kappa_x, \kappa_y) \in \mathcal{D} \times \mathcal{D}$, the discretized plane-waves in (13) and (14) are defined within the lattice ellipses (e.g. [2, Fig. 1])

$$\mathcal{E}_s = \left\{ (m_x, m_y) \in \mathbb{Z}^2 : \left(\frac{m_x \lambda}{L_{S,x}}\right)^2 + \left(\frac{m_y \lambda}{L_{S,y}}\right)^2 \leq 1 \right\} \quad (16)$$

$$\mathcal{E}_r = \left\{ (\ell_x, \ell_y) \in \mathbb{Z}^2 : \left(\frac{\ell_x \lambda}{L_{R,x}}\right)^2 + \left(\frac{\ell_y \lambda}{L_{R,y}}\right)^2 \leq 1 \right\} \quad (17)$$

at the source and receiver, respectively. We call $n_s = |\mathcal{E}_s|$ and $n_r = |\mathcal{E}_r|$ the cardinalities of the sets \mathcal{E}_s and \mathcal{E}_r , respectively, and notice that they can be computed by counting the number of lattice points falling into the 2D ellipses in (16) and (17). These are given by [2]

$$n_s = \left\lceil \frac{\pi}{\lambda^2} L_{S,x} L_{S,y} \right\rceil + o\left(\frac{L_{S,x} L_{S,y}}{\lambda^2}\right) \quad \text{and} \quad n_r = \left\lceil \frac{\pi}{\lambda^2} L_{R,x} L_{R,y} \right\rceil + o\left(\frac{L_{R,x} L_{R,y}}{\lambda^2}\right) \quad (18)$$

where $o(\cdot)$ terms can be neglected under Assumption 1. With the above definitions at hand, Theorem 2 is given.

Theorem 2. [Fourier plane-wave series expansion] The channel response $h(\mathbf{r}, \mathbf{s})$ between any $\mathbf{r} \in V_R$ and $\mathbf{s} \in V_S$ can be approximately described by a 4D Fourier plane-wave series expansion:

$$h(\mathbf{r}, \mathbf{s}) \approx \sum_{(\ell_x, \ell_y) \in \mathcal{E}_r} \sum_{(m_x, m_y) \in \mathcal{E}_s} a_r(\ell_x, \ell_y, \mathbf{r}) H_a(\ell_x, \ell_y, m_x, m_y) a_s(m_x, m_y, \mathbf{s}) \quad (19)$$

with random Fourier coefficients

$$H_a(\ell_x, \ell_y, m_x, m_y) \sim \mathcal{N}_{\mathbb{C}}\left(0, \sigma^2(\ell_x, \ell_y, m_x, m_y)\right) \quad (20)$$

which are statistically independent, circularly-symmetric, complex-Gaussian random variables, each having variance $\sigma^2(\ell_x, \ell_y, m_x, m_y)$ given by

$$\sigma^2(\ell_x, \ell_y, m_x, m_y) = \frac{1}{(2\pi)^4} \iiint_{\mathcal{S}_s(m_x, m_y) \times \mathcal{S}_r(\ell_x, \ell_y)} S(k_x, k_y, \kappa_x, \kappa_y) dk_x dk_y d\kappa_x d\kappa_y \quad (21)$$

where the sets $\mathcal{S}_s(m_x, m_y)$ and $\mathcal{S}_r(\ell_x, \ell_y)$ are defined as

$$\left\{ \left[\frac{2\pi m_x}{L_{S,x}}, \frac{2\pi(m_x+1)}{L_{S,x}} \right] \times \left[\frac{2\pi m_y}{L_{S,y}}, \frac{2\pi(m_y+1)}{L_{S,y}} \right] \right\} \quad (22)$$

$$\left\{ \left[\frac{2\pi \ell_x}{L_{R,x}}, \frac{2\pi(\ell_x+1)}{L_{R,x}} \right] \times \left[\frac{2\pi \ell_y}{L_{R,y}}, \frac{2\pi(\ell_y+1)}{L_{R,y}} \right] \right\} \quad (23)$$

and are essentially determined by the xy -spatial resolution of the surfaces.

Proof. The proof is articulated in two parts. The first part provides a discrete approximation of the Fourier plane-wave representation (4) over a fixed set of directions. This is given in Appendix and extends the proof in [3, App. IV.A] for the receiver only. The second part is given in Appendix and computes the variances of the Fourier coefficients for a generic non-isotropic scenario. Hence, it extends [3, App. IV.C] valid for isotropic scattering. \square

The above theorem generates a periodic random field that well approximates $h(\mathbf{r}, \mathbf{s})$ over its fundamental periods $(r_x, r_y) \in [0, L_{R,x}] \times [0, L_{R,y}]$ and $(s_x, s_y) \in [0, L_{S,x}] \times [0, L_{S,y}]$ through the Fourier plane-wave series expansion in (19). For the source and receive arrays illustrated in Fig. 1 of xy -dimensions $L_{S,x}, L_{S,y}$ and $L_{R,x}, L_{R,y}$, the spatial replicas generated by (19) are non-overlapping; hence, the spatial aliasing condition is always satisfied. The periodic random field in (19) is decomposed into the fixed discretized plane-waves in (13) and (14), which are weighted by the random coefficients $H_a(\ell_x, \ell_y, m_x, m_y)$. The approximation error in (19) reduces as $\min(L_{S,x}, L_{S,y})/\lambda$ and $\min(L_{R,x}, L_{R,y})/\lambda$ become large [3], and vanishes as $\min(L_{S,x}, L_{S,y})/\lambda \rightarrow \infty$ and $\min(L_{R,x}, L_{R,y})/\lambda \rightarrow \infty$ jointly – when the two representations in (4) and (19) coincide. Hence, it provides an accurate channel description under Assumption 1. Notice that (19) is perfectly convergent as $S(k_x, k_y, \kappa_x, \kappa_y)$ in (11) is singularly-integrable [3], [21].

B. Physical considerations

An intuitive physical interpretation of the Fourier plane-wave series expansion in Theorem 2 is obtained by comparing (19) to its continuous counterpart (4). The continuum incident $a_s(\kappa_x, \kappa_y, \mathbf{s})$ and received $a_r(k_x, k_y, \mathbf{r})$ plane-waves are replaced by their discretized versions $a_s(m_x, m_y, \mathbf{s})$ and $a_r(\ell_x, \ell_y, \mathbf{r})$, respectively. Physically, this implies that only a finite number of plane-waves

carries the channel information available between two planar arrays of compact size. Consequently, the continuous angular response $H_a(k_x, k_y, \kappa_x, \kappa_y)$ is replaced by $\{H_a(\ell_x, \ell_y, m_x, m_y)\}$, which, as illustrated in Fig. 2(a), describe the channel coupling between every pair of source $\mathcal{S}_s(m_x, m_y)$ and receive $\mathcal{S}_r(\ell_x, \ell_y)$ angular sets pointed by the above discretized plane-waves. For this reason, we call $\{H_a(\ell_x, \ell_y, m_x, m_y)\}$ the *coupling coefficients* (e.g., [26]). By inspection of (22) and (23), the size of each angular set is inversely proportional to the size of arrays. This is a well known property: spatially larger arrays have higher angular resolution. Since the angular sets provide a non-overlapping partition of the support $\mathcal{D} \times \mathcal{D}$, it follows that

$$P_h = \sum_{(\ell_x, \ell_y) \in \mathcal{E}_r} \sum_{(m_x, m_y) \in \mathcal{E}_s} \sigma^2(\ell_x, \ell_y, m_x, m_y). \quad (24)$$

Notice that the variances are always bounded since the integrand in (21) is singularly-integrable [3], [21]. If P_h is normalized to unity, then the variances can be regarded as a *discrete angular power distribution*; that is, $\sigma^2(\ell_x, \ell_y, m_x, m_y)$ specifies the fraction of channel power that is transferred from $\mathcal{S}_s(m_x, m_y)$ to $\mathcal{S}_r(\ell_x, \ell_y)$. The strength of the coupling coefficients is not all equal and depends jointly by the array sizes and scattering mechanism. This joint combination determines two key factors: the *number of parallel channels* and the *level of diversity*. The former is specified by the number of source and receive angular sets that have that are coupled, and will provide the DoF of the electromagnetic channel as it will be elaborated later on. The latter is determined by the number of receive angular sets that couple with each source angular set. Indeed, radiating towards specific angular directions at the source may illuminate several angular directions at the receiver. As an example, in Fig. 2(b) the coupling coefficients are arranged in matrix form. Three distinct angular sets are activated by the source (orange, blue, and green) whose radiated power is transferred to six angular sets at receiver. The number of parallel channels is three and the level of diversity is three (orange), two (blue), and one (green), respectively. A possible way to measure the coupling coefficients and their strength from spatial realizations of the channel is described later on. An analytical method for their modelling and computation is described next.

C. Physical modelling of coupling coefficients

In Appendix, after a change of integration variables in (21) from wavenumber coordinates $(k_x, k_y, \kappa_x, \kappa_y)$ to spherical coordinates $(\theta_r, \phi_r, \theta_s, \phi_s)$ (i.e., elevation and azimuth angles) we obtain

$$\sigma^2(\ell_x, \ell_y, m_x, m_y) = \iiint_{\Omega_s(m_x, m_y) \times \Omega_r(\ell_x, \ell_y)} A^2(\theta_r, \phi_r, \theta_s, \phi_s) d\Omega_s d\Omega_r \quad (25)$$

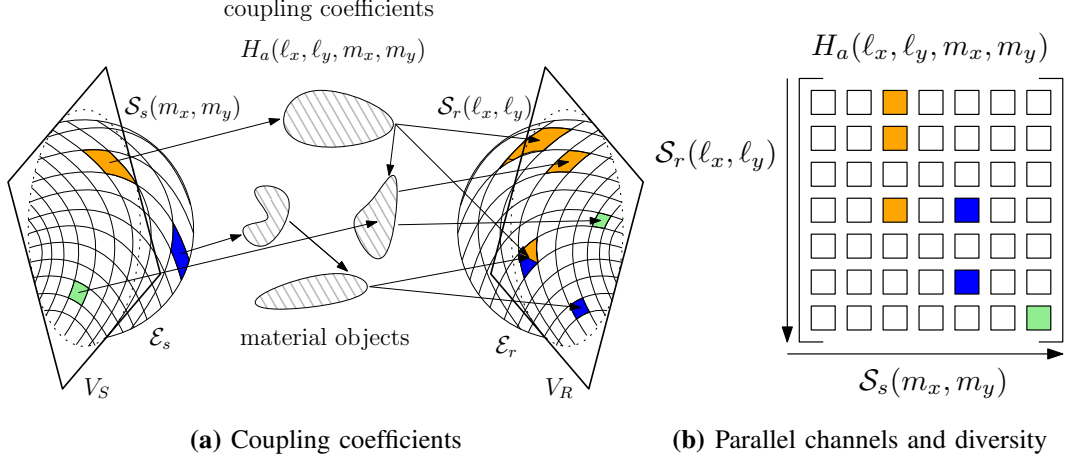


Fig. 2. Physical interpretation of the Fourier plane-wave series expansion in Theorem 2.

where $\Omega_r(\ell_x, \ell_y)$ and $\Omega_s(m_x, m_y)$ are defined in (69) and $d\Omega_r = \sin \theta_r d\theta_r d\phi_r$ and $d\Omega_s = \sin \theta_s d\theta_s d\phi_s$. Clearly, $A^2(\theta_r, \phi_r, \theta_s, \phi_s)$ represents the average angular power transfer in spherical coordinates, which determines the fraction of power transmitted onto $\Omega_s(m_x, m_y)$ and received over $\Omega_r(\ell_x, \ell_y)$. This shows that power transfer is thus generally coupled between arrays.

Next, we illustrate a few simple, but insightful, examples to model $A(\theta_r, \phi_r, \theta_s, \phi_s)$ that account for some specific propagation conditions. The simplest choice to compute (25) is to assume $A^2(\theta_r, \phi_r, \theta_s, \phi_s) = 1$, which corresponds to isotropic propagation. In this case, the scattering naturally decouples and (25) becomes

$$\sigma^2(\ell_x, \ell_y, m_x, m_y) = \sigma_s^2(m_x, m_y) \sigma_r^2(\ell_x, \ell_y) \quad (26)$$

where $\sigma_s^2(m_x, m_y)$ and $\sigma_r^2(\ell_x, \ell_y)$ account for the power transfer at source and receiver, separately. Under isotropic scattering, these can be computed in closed-form [3, App. IV.C] and physically correspond to the solid angles. At the receiver, this is given by

$$\sigma_r^2(\ell_x, \ell_y) = |\Omega_r(\ell_x, \ell_y)| = \iint_{\Omega_r(\ell_x, \ell_y)} \sin \theta_r d\theta_r d\phi_r \quad (27)$$

which is uniquely determined by the xy -spatial resolution of the arrays. A direct consequence of (26) is that the fraction of received channel power is the same irrespective from where it is emanated. This tends to result into an optimistic assessment of the number of parallel channels and the level of diversity [24, Sec. 3.6]. A simple way to model non-isotropic propagation conditions is to assume the channel power transfer to be clustered around some $N_c \geq 1$ modal propagation directions and distributed uniformly within each cluster angular region [16, Sec. 2]. This implies to model the spectral factor as a bounded piecewise constant function over non-overlapped angular sets. In this case, $\sigma^2(\ell_x, \ell_y, m_x, m_y)$ is still decoupled with $\sigma_r^2(\ell_x, \ell_y) = \iint_{\Omega_r(\ell_x, \ell_y) \cap \Theta_r} \sin \theta_r d\theta_r d\phi_r$

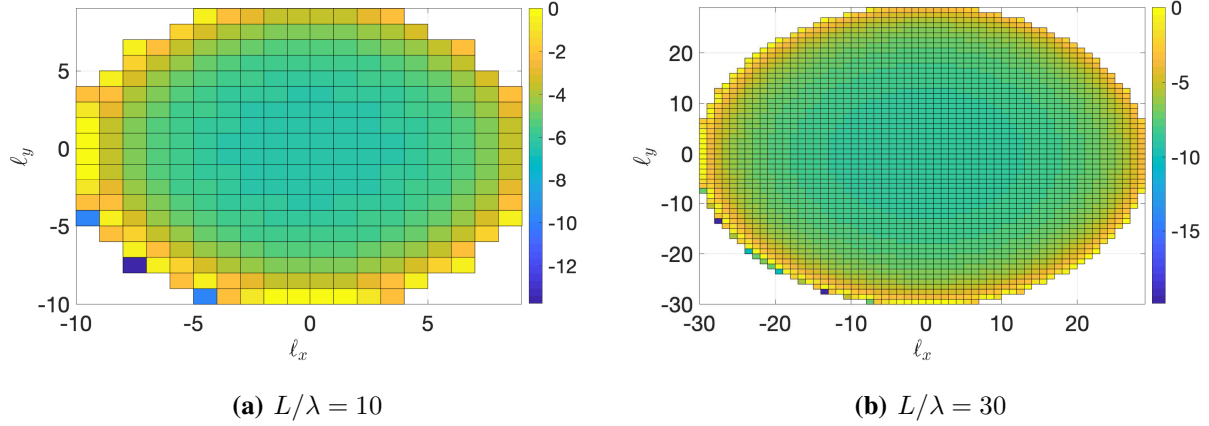


Fig. 3. Normalized (to their maximum value) strength of coupling coefficients $N_r \sigma_r^2(\ell_x, \ell_y)$ (in dB) for a squared array of sizes $L/\lambda = \{10, 30\}$ with isotropic scattering.

where $\Theta_r \subseteq \mathcal{S}_+$ are the union of all cluster angular regions. Unlike the isotropic case, the coupling coefficients are determined by the array spatial resolution and the scattering mechanism jointly; they are non-zero only if $\Omega_s(m_x, m_y)$ and $\Omega_r(\ell_x, \ell_y)$ are (at least partially) subtended by the scattering clusters. A generalized version of the model in [16] is obtained by choosing $A^2(\theta_r, \phi_r, \theta_s, \phi_s) = A_r^2(\theta_r, \phi_r) A_s^2(\theta_s, \phi_s)$ with $A_s(\theta_s, \phi_s)$ and $A_r(\theta_r, \phi_r)$ varying arbitrarily. This yields

$$\sigma_r^2(\ell_x, \ell_y) = \iint_{\Omega_r(\ell_x, \ell_y)} A_r^2(\theta_r, \phi_r) \sin \theta_r d\theta_r d\phi_r. \quad (28)$$

A good trade-off between tractability and accuracy is offered by the mixture of 3D von Mises-Fisher (vMF) family of angular density functions [21, Sec. V]. At receiver, e.g., it yields

$$A_r^2(\theta_r, \phi_r) = \sum_{i=1}^{N_c} w_i p_{r,i}(\theta_r, \phi_r) \quad (29)$$

with weights $w_i \geq 0$ such that $\sum_i w_i = 1$ and $p_{r,i}(\theta_r, \phi_r) = c(\alpha_i) e^{\alpha_i (\sin \theta \sin \mu_{\theta,i} \cos(\phi - \mu_{\phi,i}) + \cos \theta \cos \mu_{\theta,i})}$. Here, $c(\alpha_i) = \alpha_i / (4\pi \sinh \alpha_i)$ is a normalization constant, $\{\mu_{\theta,i}, \mu_{\phi,i}\}$ represent the elevation and azimuth angles of the modal direction and α_i is the so-called concentration parameter. The former specifies the propagation direction around which the power is concentrated while the latter determines the concentration of angular power, that is, as α increases the density becomes more concentrated around its modal direction. This is directly related to the circular variance $\nu^2 \in [0, 1]$ of each cluster [21, Eqs. (77)–(78)], which, in turn, determines the angular spread of the channel $\sigma_a \in [0^\circ, 360^\circ]$. Notice that the isotropic case is obtained by setting $N_c = 1$ and $\alpha_1 = 0$.

Assume symmetric spectral factors, i.e., $A_r(\theta_r, \phi_r) = A_s(\theta_s, \phi_s)$ and focus on the receive only. Assume also $L_{R,x} = L_{R,y} = L$ with $L/\lambda = \{10, 30\}$. Based on (18), there are essentially $n_r \approx \lfloor \pi(L/\lambda)^2 \rfloor = \{314, 2827\}$ angular sets. Under isotropic scattering, the normalized variances

$N_r \sigma_r^2(\ell_x, \ell_y)$ in (28) are plotted in Fig. 3. As expected, the size of each angular set reduces as L increases due to a higher angular resolution of the array. The non-zero coupling coefficients are exactly $n_r = \{344, 2928\}$ and only distributed within the lattice ellipse \mathcal{E}_r in (17). They have a bowl-shaped behavior and thus they are not all equal even under isotropic scattering. This observation will be used in Section IV-B to conclude that an electromagnetic random MIMO channel must *necessarily* exhibits spatial correlation.

The non-isotropic propagation is considered in Fig. 4. Here, we have $N_c = 2$ with $\mu_\theta = \{30^\circ, 10^\circ\}$, $\mu_\phi = \{15^\circ, 180^\circ\}$ and α such that $\nu^2 = \{.01, .005\}$, which roughly corresponds to $\sigma_a = \{15^\circ, 11^\circ\}$. The coupling coefficients are still non-zero within the lattice ellipse \mathcal{E}_r in (17) but, unlike Fig. 3, they achieve higher values around the modal directions. Compared to the isotropic case, a reduced number, say $n'_r < n_r$, of coupling coefficients is significant. Inspired by the three-sigma rule for Gaussian distributions, n'_r may be computed as the number of angular sets that are sufficient to capture the 99.7% of the total channel power (24). This yields $n'_r = 21 + 14 = 35$ and $n'_r = 145 + 84 = 229$ for Fig. 4(a) and Fig. 4(b), respectively.

D. Connection to Karhunen-Loeve expansion

Let $h(t)$ be a band-limited stationary random process of bandwidth B that is observed over a time interval $[0, T]$. Asymptotically as $BT \gg 1$, the eigenfunctions of its Karhunen-Loeve expansion approach complex harmonics oscillating at an integer multiple of the fundamental frequency $1/T$ and the eigenvalues' power are obtained by sampling the power spectral density of the process at these frequencies [22, Sec. 3.4]. Next, we show how this fundamental result applies to spatially-stationary electromagnetic channel fields, which we recall to be circularly band-limited in the spatial-frequency domain with maximum bandwidth $\pi\kappa^2$ [3], [21].

Consider the two 2D spatial-frequency Fourier harmonics

$$\phi_s(m_x, m_y, s_x, s_y) = e^{j\left(\frac{2\pi}{L_{S,x}}m_x s_x + \frac{2\pi}{L_{S,y}}m_y s_y\right)} \quad (30)$$

$$\phi_r(\ell_x, \ell_y, r_x, r_y) = e^{j\left(\frac{2\pi}{L_{R,x}}\ell_x r_x + \frac{2\pi}{L_{R,y}}\ell_y r_y\right)} \quad (31)$$

with fundamental periods $(r_x, r_y) \in [0, L_{R,x}] \times [0, L_{R,y}]$ and $(s_x, s_y) \in [0, L_{S,x}] \times [0, L_{S,y}]$. For any fixed pair of s_z and r_z with $r_z > s_z$, the discretized plane-waves in (19) correspond to two

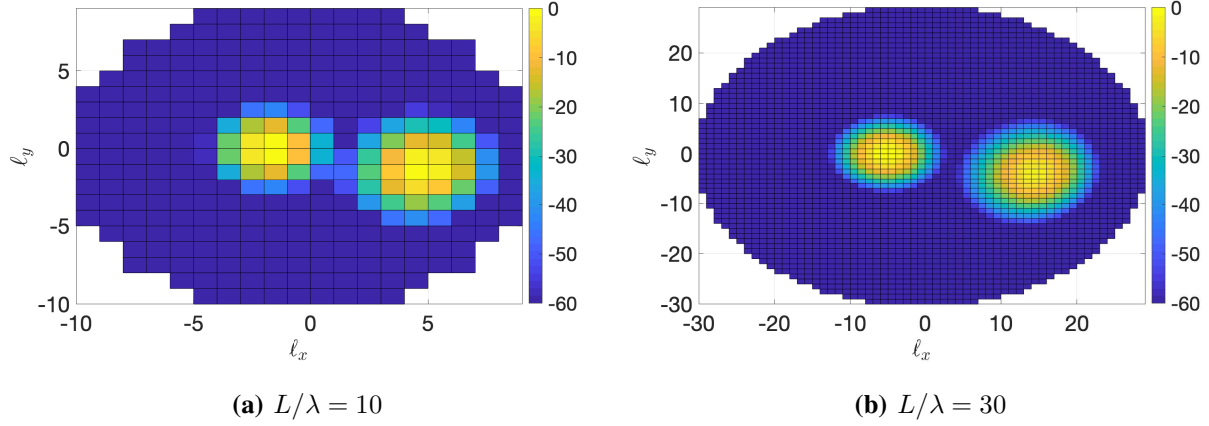


Fig. 4. Normalized (to their maximum value) strength of coupling coefficients $N_r \sigma_r^2(\ell_x, \ell_y)$ (in dB) for $L/\lambda = \{10, 30\}$ with non-isotropic scattering. The mixture of 3D vMF angular density function is used with $N_c = 2$, $\mu_\theta = \{30^\circ, 10^\circ\}$, $\mu_\phi = \{15^\circ, 180^\circ\}$ and α such that $\nu^2 = \{.01, .005\}$, which roughly corresponds to an angular spread of $\sigma_a = \{15^\circ, 11^\circ\}$.

phase-shifted versions of the two 2D spatial-frequency Fourier harmonics, i.e.,

$$a_s(m_x, m_y, \mathbf{s}) = \phi_s^*(m_x, m_y, s_x, s_y) e^{-j\gamma_s(m_x, m_y)s_z} \quad (32)$$

$$a_r(\ell_x, \ell_y, \mathbf{r}) = \phi_r(\ell_x, \ell_y, r_x, r_y) e^{j\gamma_r(\ell_x, \ell_y)r_z}. \quad (33)$$

Hence, we can rewrite (19) as

$$h(\mathbf{r}, \mathbf{s}) \approx \sum_{(\ell_x, \ell_y) \in \mathcal{E}_r} \sum_{(m_x, m_y) \in \mathcal{E}_s} H(\ell_x, \ell_y, m_x, m_y; r_z, s_z) \phi_r(\ell_x, \ell_y, r_x, r_y) \phi_s^*(m_x, m_y, s_x, s_y) \quad (34)$$

where we have defined

$$\tilde{H}(\ell_x, \ell_y, m_x, m_y; r_z, s_z) = H_a(\ell_x, \ell_y, m_x, m_y) e^{-j\gamma_s(m_x, m_y)s_z} e^{j\gamma_r(\ell_x, \ell_y)r_z}. \quad (40)$$

Notice that $\tilde{H}(\ell_x, \ell_y, m_x, m_y; r_z, s_z)$ and $H_a(\ell_x, \ell_y, m_x, m_y)$ are statistically equivalent. The spatial correlation function of $h(\mathbf{r}, \mathbf{s})$ is $c_h(\mathbf{r}, \mathbf{s}) = \mathbb{E}\{h(\mathbf{r} + \mathbf{r}', \mathbf{s} + \mathbf{s}')h^*(\mathbf{r}', \mathbf{s}')\}$. By using (34) and (40), it can be approximated as

$$c(\mathbf{r}, \mathbf{s}) \approx \sum_{(\ell_x, \ell_y) \in \mathcal{E}_r} \sum_{(m_x, m_y) \in \mathcal{E}_s} \sigma^2(\ell_x, \ell_y, m_x, m_y) \phi_r(\ell_x, \ell_y, r_x, r_y) \phi_s^*(m_x, m_y, s_x, s_y). \quad (41)$$

The closed-form expression (41) can be regarded as the *asymptotic* Hilbert-Schmidt decomposition [27, Sec. 3.4] of the self-adjoint correlation kernel function $c_h(\mathbf{r}, \mathbf{s})$; that is, $\{\phi_s(m_x, m_y, \mathbf{s})\}$ and $\{\phi_r(\ell_x, \ell_y, \mathbf{r})\}$ are the complete (non-normalized) orthonormal basis sets of eigenfunctions, and $\{\sigma^2(\ell_x, \ell_y, m_x, m_y)\}$ is the sequence of non-negative real-valued eigenvalues. In analogy with the time-domain stationary case [22], the expansion of $h(\mathbf{r}, \mathbf{s})$ over the above basis sets

of eigenfunctions yields (34), which is the *asymptotic* Karhunen-Loeve expansion [27, Sec. 6.4] of a spatially-stationary random electromagnetic field. As for time-domain processes, the asymptotic regime is achieved under Assumption 1. Unlike the time-domain, the spatial case exhibits a lower-dimensionality since the 6D power spectral density of $h(\mathbf{r}, \mathbf{s})$ is impulsive and defined on a double sphere of radius κ [11], [21]. Another key difference is that we do not sample at integer multiples of the fundamental spatial frequencies but rather (11) over a neighbourhood of these frequencies. As shown in Appendix, this is because (11) is singularly-integrable.

IV. STOCHASTIC ELECTROMAGNETIC MIMO CHANNEL MODEL

From (3), the MIMO matrix is approximated by sampling the series representation in (19) as

$$\mathbf{H} = \sqrt{N_r N_s} \sum_{\ell_x, \ell_y} \sum_{m_x, m_y} H_a(\ell_x, \ell_y, m_x, m_y) \mathbf{a}_r(\ell_x, \ell_y) \mathbf{a}_s^H(m_x, m_y) \quad (42)$$

where $\mathbf{a}_r(\ell_x, \ell_y)$ and $\mathbf{a}_s(m_x, m_y)$ represents the (normalized) discrete-space source and receive array responses with entries

$$[\mathbf{a}_s(m_x, m_y)]_j = \frac{1}{\sqrt{N_s}} a_s(m_x, m_y, s_{x_j}, s_{y_j}, s_z) \quad (43)$$

$$[\mathbf{a}_r(\ell_x, \ell_y)]_i = \frac{1}{\sqrt{N_r}} a_r(\ell_x, \ell_y, r_{x_j}, r_{y_j}, r_z). \quad (44)$$

Different array geometries and antenna spacings may have a marked effect on \mathbf{H} and its statistics. To guarantee that no information is lost by sampling $h(\mathbf{r}, \mathbf{s})$, the Nyquist condition in the spatial domain must be satisfied. From Corollary 1, $h(\mathbf{r}, \mathbf{s})$ is a circularly-bandlimited channel with maximum bandwidth $\pi\kappa^2$, for any scattering environment. If $h(\mathbf{r}, \mathbf{s})$ is uniformly sampled with spacings $\Delta_{R,x}, \Delta_{R,y}$, the Nyquist condition is met when $\min(\Delta_{R,x}, \Delta_{R,y}) \leq \lambda/2$ (e.g., [3, Sec. V], [2]). In other words, no information is lost when the receive array is equipped with

$$N_r \geq \frac{4L_{R,x}L_{R,y}}{\lambda^2} \geq n_r \quad (45)$$

antenna elements under Assumption 1. A similar condition must be satisfied at the source array. Both are assumed in the remainder.

Remark 3. *We stress that sampling at Nyquist's rate (or higher) ensures no loss of channel information. This allows to fully exploit the propagation characteristics offered by an electromagnetic channel and to design a system that ultimately exploits all its degrees of freedom. This is exactly the scope of a Holographic MIMO system.*

There is a 2D counterpart to the 3D theory presented in this paper, where linear arrays rather than rectangular ones are considered; see [21, Sec VIII]. In this case, a similar representation of \mathbf{H} is obtained, which is reminiscent of the virtual channel representation pioneered in [14], [15]. Both provide an angular decomposition of the 2D MIMO channel over a fixed sets of directions and are specified by statistically-independent random coefficients. However, the Fourier plane-wave model differs from the virtual channel representation in several aspects: (i) it is derived from the physics principles of wave propagation and it is thus valid also in the near-field propagation region; (ii) it models planar and volumetric arrays of arbitrary geometry operating in a general 3D propagation environment; (iii) it reveals the lower-dimensionality of the angular description for electromagnetic channels, i.e., only $n_r n_s$ (rather than $N_r N_s$) coupling coefficients contain the essential information; (iv) it supports the physical model with a statistical analysis that is built upon a closed-form expression of the power spectral density of a random electromagnetic channel.

A. Karhunen-Loeve expansion

Call $\phi_s(m_x, m_y) \in \mathbb{C}^{N_s}$ the vector with entries $[\phi_s(m_x, m_y)]_j = \frac{1}{\sqrt{N_s}} \phi_s(m_x, m_y, s_{x_j}, s_{y_j})$ for $j = 1, \dots, N_s$. Similarly, $\phi_r(\ell_x, \ell_y) \in \mathbb{C}^{N_r}$ has entries $[\phi_r(\ell_x, \ell_y)]_i = \frac{1}{\sqrt{N_r}} \phi_r(\ell_x, \ell_y, r_{x_i}, r_{y_i})$ for $i = 1, \dots, N_r$. Hence, (42) can equivalently be rewritten as

$$\mathbf{H} = \sqrt{N_r N_s} \sum_{(\ell_x, \ell_y)} \sum_{(m_x, m_y)} \tilde{H}(\ell_x, \ell_y, m_x, m_y; r_z, s_z) \phi_r(\ell_x, \ell_y) \phi_s^H(m_x, m_y) \quad (46)$$

where the channel coefficients $\tilde{H}(\ell_x, \ell_y, m_x, m_y; r_z, s_z)$ given in (40) are the coupling coefficients between the n_s angle sets at the source and the n_r angle sets at the receiver. Since $\{\phi_s(m_x, m_y)\}$ and $\{\phi_r(\ell_x, \ell_y)\}$ constitute a set of orthonormal discrete basis functions, and the coupling coefficients $\tilde{H}(\ell_x, \ell_y, m_x, m_y; r_z, s_z)$ are Gaussian independent, (46) can be regarded as the Karhunen-Loeve expansion of the electromagnetic MIMO channel [28], which well shows that \mathbf{H} has at most rank $n_r n_s$ as it is constructed as a sum of rank-1 isometric matrices. Notice that orthonormal discrete basis functions are fixed; they do not depend on the statistics of \mathbf{H} . The strength of each coupling coefficient specifies the mean amount of energy that is coupled from the (ℓ_x, ℓ_y) th receive basis function and the (m_x, m_y) th source basis function. The average channel power is thus $\mathbb{E}\{\text{tr}(\mathbf{H}^H \mathbf{H})\} = \sum_{\ell_x, \ell_y} \sum_{m_x, m_y} \sigma^2(\ell_x, \ell_y, m_x, m_y) = P_h$ in (24).

Denote Φ_s and Φ_r the deterministic matrices collecting the n_s and n_r vectors $\{\phi_s(m_x, m_y)\}$ and $\{\phi_r(\ell_x, \ell_y)\}$, respectively. Also, let γ_s and γ_r be the column vectors containing the n_s and n_r coefficients $\gamma_s(m_x, m_y)$ and $\gamma_r(\ell_x, \ell_y)$, respectively. The following lemma is thus obtained.

Lemma 1. For any s_z and $r_z > s_z$, the MIMO channel matrix is obtained as

$$\mathbf{H} = \Phi_r \tilde{\mathbf{H}} \Phi_s^H \quad (47)$$

where $\tilde{\mathbf{H}} = e^{j\Gamma_r} \mathbf{H}_a e^{-j\Gamma_s}$. Here, $e^{j\Gamma_r}$ and $e^{-j\Gamma_s}$ are diagonal matrices with $\Gamma_r = \text{diag}(\gamma_r r_z)$ and $\Gamma_s = \text{diag}(\gamma_s s_z)$, and $\mathbf{H}_a \in \mathbb{C}^{n_r \times n_s}$ is the angular random matrix obtained as

$$\mathbf{H}_a = \Sigma \odot \mathbf{W} \quad (48)$$

where $\Sigma \in \mathbb{R}_+^{n_r \times n_s}$ collects the $n_r n_s$ scaled standard deviations $\{\sqrt{N_s N_r} \sigma(\ell_x, \ell_y, m_x, m_y)\}$ and $\mathbf{W} \in \mathbb{C}^{n_r \times n_s}$ is the matrix with i.i.d. circularly-symmetric, complex-Gaussian random entries.

Since Φ_s and Φ_r are semi-unitary matrices, i.e., $\Phi_s^H \Phi_s = \mathbf{I}_{n_s}$ and $\Phi_r^H \Phi_r = \mathbf{I}_{n_r}$, and $\tilde{\mathbf{H}}$ is statistically equivalent to \mathbf{H}_a , the above lemma shows that the angular matrix \mathbf{H}_a is *semi-unitarily equivalent* to \mathbf{H} in the sense that the most significant $\min(n_r, n_s)$ singular values of the two matrices are identical. This property is reminiscent to the unitary-independent-unitary (UIU) MIMO channel model [28, Eq. (1)], where the channel is decomposed in terms of N_r - and N_s -dimensional unitary matrices. However, as $n_s \ll N_s$ and $n_r \ll N_r$, we have that channel models in the UIU form represent a highly redundant description of the electromagnetic channel. In other words, the provided Fourier plane-wave model yields a physics-based *low-rank approximation* of \mathbf{H} with respect to fixed spatial basis matrices that are independently defined by the array geometry at each end. The low-rank property of electromagnetic channels is even more visible under non-isotropic propagation conditions when only a subset of coupling coefficients is significant, as discussed in Section III-C. Since the coupling coefficients are independent, the rows and columns of \mathbf{H}_a are linearly independent with probability 1 except for those that are identically zero [28]. Particularly, if we denote with $n'_s \leq n_s$ and $n'_r \leq n_r$ the number of rows and columns of \mathbf{H}_a that are not identically zero, the number of singular values are

$$\text{rank}(\mathbf{H}_a) = \min(n'_s, n'_r) \leq \min(n_s, n_r) \quad (49)$$

which corresponds to the DoF of the channel. As observed in [16], the DoF does not scale with the number of antenna elements but depends on the scattering environment and array sizes jointly. Clearly, the number of DoF equals the upper bound in (49) when non-zero power is received from all angular sets; that is, under isotropic scattering. In this case, the DoF per m^2 are given by π/λ^2 [2]. If not, the DoF diminishes according to the angular spread of the channel.

With uniform sampling, the semi-unitary matrices Φ_s and Φ_r become two-dimensional inverse discrete Fourier transform (IDFT) matrices. Notice that whole randomness of \mathbf{H} is fully embedded into \mathbf{H}_a whereas the deterministic matrices $\Phi_s^H e^{-j\Gamma_s}$ and $\Phi_r e^{j\Gamma_r}$ change the domain of representation from angular to spatial at source and receiver, respectively. Particularly, the two matrices $e^{j\Gamma_r}$ and $e^{-j\Gamma_s}$ are known in physics as *propagators* or *migration filters*, and are fully determined by the array geometry and wavelength. They contain the whole effect due to wave propagation along the z -axis. Note that this effect is fully deterministic and known a priori; hence, there is no channel information that can be captured along the z -dimension. As observed in [29], the world – at both source and receiver – has only an apparent 3D informational structure, which is subject to a 2D representation. A key consequence of this observation is that a 3D volumetric array offers no extra DoF over a 2D planar array (e.g., [2], [26]).

The MIMO channel model (47) does not have a Kronecker structure. However, this naturally arises if the separability propagation condition (26) is imposed.

Corollary 2 (Separable model). *If the scattering is separable, (48) becomes*

$$\mathbf{H}_a = \text{diag}(\boldsymbol{\sigma}_r) \mathbf{W} \text{diag}(\boldsymbol{\sigma}_s) \quad (50)$$

where $\boldsymbol{\sigma}_r \in \mathbb{R}_+^{n_r}$ and $\boldsymbol{\sigma}_s \in \mathbb{R}_+^{n_s}$ collect $\{\sqrt{N_r} \sigma_r(\ell_x, \ell_y)\}$ and $\{\sqrt{N_s} \sigma_s(m_x, m_y)\}$, respectively.

Proof. Under the separability condition (26), Σ in (48) becomes $\Sigma = \boldsymbol{\sigma}_r \mathbf{1}_{n_s}^T \odot \mathbf{1}_{n_r}^T \boldsymbol{\sigma}_s^T$ and thus $\mathbf{H}_a = (\boldsymbol{\sigma}_r \mathbf{1}_{n_s}^T) \odot \mathbf{W} \odot (\mathbf{1}_{n_r}^T \boldsymbol{\sigma}_s^T)$. By applying the matrix identity $(\mathbf{a}\mathbf{b}^H) \odot \mathbf{X} = \text{diag}(\mathbf{a})\mathbf{X}\text{diag}(\mathbf{a})^H$, we obtain $\mathbf{H}_a = \text{diag}(\boldsymbol{\sigma}_r) \mathbf{W} \text{diag}(\boldsymbol{\sigma}_s)$ which used in (47) yields the desired result. \square

A similar model was proposed in [13, Eq. (14) and Eq. (27d)] for a MIMO channel with linear arrays in the far-field. The model in (50) is a generalization for planar arrays in the near-field.

B. Channel Statistics

Lemma 1 gives rise to correlated Rayleigh fading (e.g., [19], [24]) where the correlation matrix (2) can be used for the description of the joint correlation properties of both ends. A detailed description of \mathbf{R} is thus in order. Since $e^{j\Gamma_r}$ and $e^{-j\Gamma_s}$ are diagonal, we may write $\tilde{\mathbf{H}}$ as $\tilde{\mathbf{H}} = \Sigma \odot (e^{j\Gamma_r} \mathbf{W} e^{-j\Gamma_s})$ where $e^{j\Gamma_r} \mathbf{W} e^{-j\Gamma_s}$ is statistically equivalent to \mathbf{W} . The correlation matrix is thus (e.g., [30])

$$\mathbf{R} = \mathbf{U} \boldsymbol{\Lambda} \mathbf{U}^H \quad (51)$$

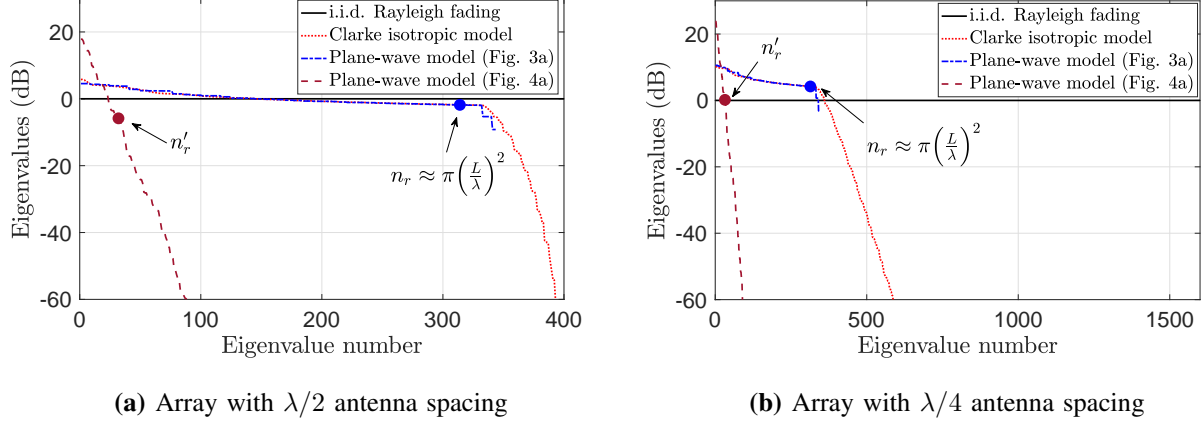


Fig. 5. Channel eigenvalues (dB) of \mathbf{R}_r reported in a descending order for a squared array of size $L/\lambda = 10$ in a setup with $\lambda/2$ - and $\lambda/4$ -spaced antenna elements (i.e., $N_r = 400$ and $N_r = 1600$). The Fourier-plane wave model for the scattering conditions in in Fig. 3(a) and Fig. 4(a) is compared to the Clarke's isotropic model and i.i.d. Rayleigh fading model.

where $\mathbf{U} = \Phi_s \otimes \Phi_r \in \mathbb{C}^{N_r N_s \times n_r n_s}$ is semi-unitary³ (i.e., $\mathbf{U}^H \mathbf{U} = \mathbf{I}_{n_s n_r}$) and

$$\boldsymbol{\Lambda} = \text{diag}(\text{vec}(\boldsymbol{\Sigma} \odot \boldsymbol{\Sigma})). \quad (52)$$

The expression (51) provides the eigendecomposition of \mathbf{R} with $(\phi_s(m_x, m_y) \otimes \phi_r(\ell_x, \ell_y))$ being the eigenvectors and $N_s N_r \sigma^2(\ell_x, \ell_y, m_x, m_y)$ being the eigenvalues. As mentioned before, the eigenvectors are fixed, not derived from the covariance of \mathbf{H} itself. Also, the eigenvalues are limited to $n_r n_s$ by physical principles. Hence, (51) provides a significant computational saving compared to its direct computation, which would require knowledge of $(N_r N_s)^2$ real-valued parameters.

As shown in [30, Eq. (6)], the correlation matrix \mathbf{R} in (51) has as a Kronecker structure on eigenmode level. If the separability condition is imposed, from (50) in Corollary 2 it follows that $\mathbf{R} = \mathbf{R}_s \otimes \mathbf{R}_r$ with receive (transmit) correlation matrix $\mathbf{R}_r = \Phi_r \text{diag}(\boldsymbol{\sigma}_r \odot \boldsymbol{\sigma}_r) \Phi_r^H \in \mathbb{C}^{N_r \times N_r}$ ($\mathbf{R}_s = \Phi_s \text{diag}(\boldsymbol{\sigma}_s \odot \boldsymbol{\sigma}_s) \Phi_s^H \in \mathbb{C}^{N_s \times N_s}$) to which correspond an eigenvalue matrix $\boldsymbol{\Lambda} = \text{diag}(\boldsymbol{\sigma}_r \odot \boldsymbol{\sigma}_r) \otimes \text{diag}(\boldsymbol{\sigma}_s \odot \boldsymbol{\sigma}_s)$. The most salient feature of the above Kronecker model is that the correlation between two transmit (receive) antennas is the same irrespective of the receive (transmit) antenna where it is observed. This is not the case for (51).

The correlation properties of \mathbf{H} depends on the eigenvalues of \mathbf{R} . For the Kronecker model in Corollary 2 with symmetric scattering, we can concentrate only on the eigenvalues of \mathbf{R}_r . These are illustrated in Fig. 5 in dB sorted in a descending order for $L/\lambda = 10$ and in a setup with $\lambda/2$ –

³The Kronecker product of semi-unitary matrices is semi-unitary.

and $\lambda/4$ -spaced antenna elements (i.e., $N_r = 400$ and $N_r = 1600$), respectively. Both isotropic and non-isotropic propagation conditions in Fig. 3(a) and Fig. 4(a) are considered. The number of significant coupling coefficients for the two cases is $n'_r = n_r \approx 314$ and $n'_r = 35$, as indicated by a circle on the corresponding curves. These determine the number of eigenvalues that carry the essential channel information. Note that, for the i.i.d. Rayleigh fading model, we have $N_r N_s$ eigenvalues equal to 1. Hence, the gap between the two is given by $N_r/n_r = \lambda^2/(\pi\Delta_{R,x}\Delta_{R,y})$ that yields roughly a $1.2\times$ and $5\times$ overall increase in the number of eigenvalues. Remarkably, this error grows quadratically with the normalized antenna spacings.

As shown in Fig. 5, the more uneven the coupling coefficients, the steeper the eigenvalues decay, which implies higher correlation. Ideally, if $\Lambda = N_s N_r \mathbf{I}_{n_s n_r}$ in (52) the channel samples would be mutually independent, thus leading to the i.i.d. Rayleigh fading model. However, this is never the case. In fact, the strengths of the coupling coefficients are not all equal even in the presence of isotropic propagation [3], as it follows from Fig. 3. This proves that an electromagnetic random MIMO channel necessarily exhibits spatial correlation [3] and implies that the i.i.d. Rayleigh fading model shall never be used to model \mathbf{H} [31]. The closest physically-tenable model to an i.i.d. Rayleigh fading is the Clarke's isotropic model [3], [11]. This is generated from the spatial correlation matrix \mathbf{R}_c whose (i, j) -th entry is $[\mathbf{R}_c]_{ij} = \text{sinc}(2d_{ij}/\lambda)$ where d_{ij} is the distance between the i -th and j -th receive antennas. As seen in Fig. 5, the Fourier plane-wave model with isotropic propagation provides us with an n_r -order low-rank approximation of Clarke's model. The error due to “discarding” $N_r - n_r$ eigenvalues is approximately 4.6% of the total channel power at $L/\lambda = 10$. This reduces to 2.3% when $L/\lambda = 30$ and approaches zero asymptotically. In terms of capacity, for $L/\lambda = 10$ we already obtain a high accuracy, as shown in [1, Fig. 2].

C. Channel generation and migration filters

The generation of the electromagnetic MIMO channel in (47) requires only knowledge of the strength of the coupling coefficients (53). If this knowledge is available, it can be generated as follows: *i*) Generate $\mathbf{W} \in \mathbb{C}^{n_r \times n_s}$ with entries $\sim \mathcal{N}_{\mathbb{C}}(0, 1)$; *ii*) Compute \mathbf{H}_a as in (48); *iii*) Compute $\tilde{\mathbf{H}}$ for any s_z and $r_z > s_z$; *iv*) Obtain \mathbf{H} (47) as $\Phi_r (\Phi_s \tilde{\mathbf{H}}^H)^H$. With uniform sampling, the matrices Φ_s and Φ_r reduce to two 2D IDFT transform. Hence, the last step has a relatively low complexity. Notice that the computation of \mathbf{H} for a different s_z or $r_z > s_z$ requires only to perform the third and fourth steps. The third step requires left- and right-multiplication by the propagators (migrators) e^{Γ_r} and $e^{-\Gamma_s}$ that are known a priori as they are fully determined by the array geometry and wavelength.

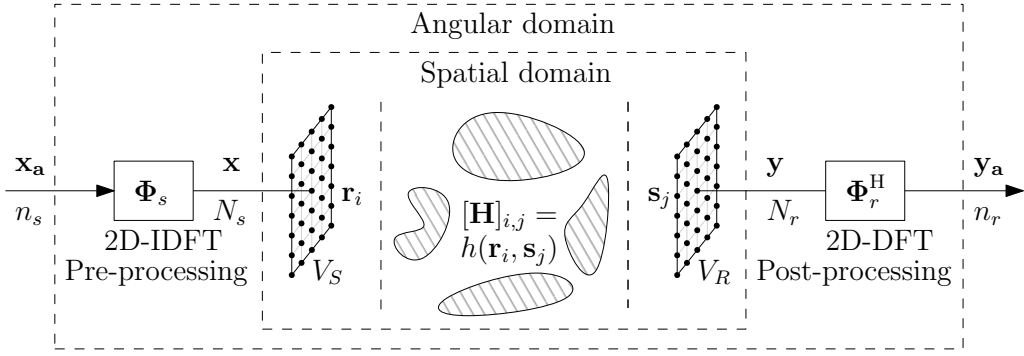


Fig. 6. Transceiver architecture for communicating over the electromagnetic MIMO channel.

Alternatively, the MIMO channel can be generated by using (51) as $\text{vec}(\mathbf{H}) = \mathbf{U}\Lambda^{1/2}\tilde{\mathbf{w}}$ where $\tilde{\mathbf{w}} \sim \mathcal{N}_{\mathbb{C}}(0, \mathbf{I}_{n_r n_s})$. This way to generate the MIMO channel should be used whenever one is interested in metrics (such as the capacity) where only the statistical equivalence between $\tilde{\mathbf{H}}$ and \mathbf{H}_a matters. In this case, the application of propagator matrices becomes irrelevant.

D. Measurements of coupling coefficients

The deterministic matrices Φ_r and Φ_s depend only on the array geometries, and thus are known. This is a useful property to estimate the coupling coefficients of \mathbf{H} . Indeed, pilot signals can be transmitted along their vectors. Hence, it is sufficient to transmit approximately $n_r n_s$ pilot signals. Notice that n_r and n_s depend on the wavelength λ . This means that the pilot resources increases with the carrier frequency.

The strength of the coupling coefficients depends exclusively on the scattering mechanisms, which evolve slowly in time compared to the fast variations of \mathbf{H} . This implies that they can be estimated with high accuracy. From (46), they are given by

$$\sigma^2(\ell_x, \ell_y, m_x, m_y) = \mathbb{E} \left\{ |\phi_r^H(\ell_x, \ell_y) \mathbf{H} \phi_s(m_x, m_y)|^2 \right\} \quad (53)$$

which provides a possible way to estimate without the need of measuring the channel matrix \mathbf{H} ; that is, transmit the signal $\phi_s(m_x, m_y)$, project the received signal onto $\phi_r(\ell_x, \ell_y)$, compute the square of the absolute value of measurement and take the average over the different measurements. Recall that only the knowledge of the $n_r n_s$ real-valued coefficients $\{\sigma^2(\ell_x, \ell_y, m_x, m_y)\}$ is needed to fully specify the correlation matrix \mathbf{R} in (51).

V. CAPACITY EVALUATION

We now use the developed channel model to numerically evaluate the capacity of the MIMO communication system in (1). From the semi-unitary equivalence between the spatial-domain and

angular-domain in Lemma 1, we have that (1) is equivalent to

$$\mathbf{y}_a = \sqrt{\text{snr}} \mathbf{H}_a \mathbf{x}_a + \mathbf{n}_a \quad (54)$$

where $\mathbf{y}_a = \Phi_r^H \mathbf{y} \in \mathbb{C}^{n_r}$ and $\mathbf{x}_a = \Phi_s^H \mathbf{x} \in \mathbb{C}^{n_s}$ denote the received and transmitted signal vectors in the angular domain, respectively. Here, snr is the signal-to-noise ratio (SNR) at the receiver that is comprehensive of the large-scale fading coefficient. Also, $\mathbf{n}_a = \Phi_r^H \mathbf{n} \in \mathbb{C}^{n_r}$ is the angular noise vector distributed as $\mathbf{n}_a \sim \mathcal{N}_{\mathbb{C}}(\mathbf{0}, \mathbf{I}_{n_r})$. Unlike (1), the entry $[\mathbf{H}_a]_{ij}$ represents the coupling coefficient between the j th angular set $\mathcal{S}_s(m_x, m_y)$ in (22) and the i th angular set $\mathcal{S}_r(\ell_x, \ell_y)$ in (23). Under the assumption $\mathbf{Q}_a = \mathbb{E}\{\mathbf{x}_a^H \mathbf{x}_a\} \leq 1$, the ergodic capacity of (54) in bit/s/Hz is

$$C = \max_{\mathbf{Q}_a: \text{tr}(\mathbf{Q}_a) \leq 1} \mathbb{E}\{\log_2 \det(\mathbf{I}_{n_r} + \text{snr} \mathbf{H}_a \mathbf{Q}_a \mathbf{H}_a^H)\}. \quad (55)$$

This is computed and quantified next under different degrees of channel state information.

Remark 4. *The transceiver architecture for communicating over the electromagnetic MIMO channel is illustrated Fig. 6. As seen, the transformation from the angular-domain to the spatial-domain (and viceversa) is fully determined by the matrices Φ_s and Φ_r^H , which depend only on the array geometries. With uniform sampling, Φ_s and Φ_r^H become two-dimensional DFT and IDFT matrices, which can be efficiently implemented in the analog domain by using a Butler matrix [32] or by means of lens antenna arrays [33]. Signal processing algorithms operate in the angular domain and thus their complexity depend on the cardinality of \mathbf{H}_a , i.e., n_r and n_s at maximum. Hence, we can operate in a regime where $N_s \gg n_s$ and $N_r \gg n_r$ without any impact on the signal processing (e.g., channel estimation, optimal signaling, coding).*

A. Perfect channel knowledge at receiver

When instantaneous channel state information is only available at the receiver, the ergodic capacity in (55) is achieved by an i.i.d. input vector \mathbf{x}_a with $\mathbf{Q}_a = \frac{1}{n_s} \mathbf{I}_{n_s}$ [34] and is given by

$$C = \sum_{i=1}^{\text{rank}(\mathbf{H}_a)} \mathbb{E} \left\{ \log_2 \left(1 + \frac{\text{snr}}{n_s} \lambda_i(\mathbf{H}_a \mathbf{H}_a^H) \right) \right\} \quad (56)$$

where $\{\lambda_i(\mathbf{A})\}$ are the eigenvalues of an arbitrary \mathbf{A} . Under separability, (56) reduces to

$$C = \sum_{i=1}^{\text{rank}(\mathbf{H}_a)} \mathbb{E} \left\{ \log_2 \left(1 + \frac{\text{snr}}{n_s} \lambda_i(\text{diag}(\boldsymbol{\sigma}_r \odot \boldsymbol{\sigma}_r) \mathbf{W} \mathbf{W}^H \text{diag}(\boldsymbol{\sigma}_s \odot \boldsymbol{\sigma}_s)) \right) \right\} \quad (57)$$

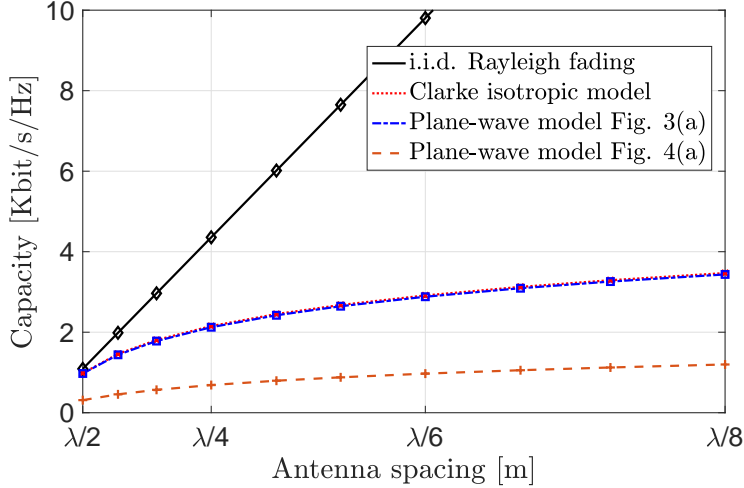


Fig. 7. Ergodic capacity in Kbit/s/Hz as a function of antenna spacing $\Delta \in [\lambda/2, \lambda/8]$ for a squared array of size $L/\lambda = 10$ and snr = 10 dB. The Fourier plane-wave model is generated by using the setting of Fig. 3(a) and Fig. 4(a).

as obtained plugging (50) into (56). Under Assumption 1, $n_s, n_r \gg 1$ and tools from random matrix theory can be used to asymptotically approximate (57) as [28, Eq. (102)]

$$C \approx \sum_{j=1}^{n_s} \log_2 \left(\frac{1 + \text{snr}[\boldsymbol{\sigma}_s \odot \boldsymbol{\sigma}_s]_j \Gamma_r}{e^{\text{snr} \Gamma_s \Gamma_r}} \right) + \sum_{i=1}^{n_r} \log_2 (1 + \text{snr}[\boldsymbol{\sigma}_r \odot \boldsymbol{\sigma}_r]_i \Gamma_s)$$

where the coefficients Γ_r, Γ_s are obtained by solving the fixed-point equations [28, Eqs. (103)–(104)]:

$$\Gamma_r = \frac{1}{n_s} \sum_{i=1}^{n_r} \frac{[\boldsymbol{\sigma}_r \odot \boldsymbol{\sigma}_r]_i}{1 + \rho[\boldsymbol{\sigma}_r \odot \boldsymbol{\sigma}_r]_i \Gamma_s} \quad \Gamma_s = \frac{1}{n_s} \sum_{j=1}^{n_s} \frac{[\boldsymbol{\sigma}_s \odot \boldsymbol{\sigma}_s]_j}{1 + \rho[\boldsymbol{\sigma}_s \odot \boldsymbol{\sigma}_s]_j \Gamma_r}. \quad (58)$$

In Fig. 7, we plot the ergodic capacity in Kbit/s/Hz as a function of antenna spacing $\Delta \in [\lambda/2, \lambda/8]$ in the same setup of Fig. 5(a) with $L/\lambda = 10$. The continuous lines are generated from (57) by using Monte Carlo simulations, whereas markers are generated according to the large-dimensional approximation in (58). A perfect match is observed although n_s, n_r are finite. Comparisons are made with the Clarke's model in which power is allocated only onto the most significant n_s eigenmodes. The perfect match with the Fourier plane-wave model validates our physical low-rank approximation under isotropic propagation conditions. The capacity with i.i.d. Rayleigh fading is also reported as reference. Compared to this model, a large gap is observed for $\Delta < \lambda/2$ due to the correlation that naturally arises among antennas when Δ decreases. This confirms that i.i.d. Rayleigh fading is highly inadequate to model the channel with planar arrays of sub-wavelength spacing. In fact, it cannot be derived from physic principles when planar arrays are considered [3]. The error in terms of DoF is inversely proportional to the square of normalized antenna spacing.

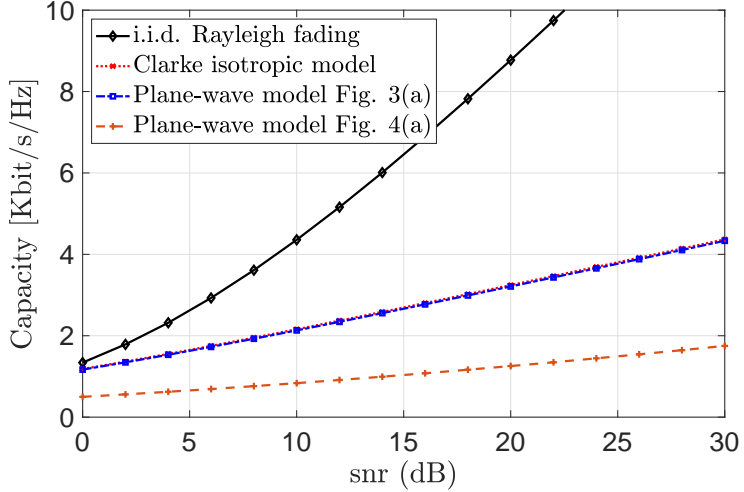


Fig. 8. Ergodic capacity C in Kbit/s/Hz as a function of snr in dB for a squared array of size $L/\lambda = 10$ in a setup with $\lambda/4$ -spaced antenna elements (i.e., $N_r = 1600$). The Fourier plane-wave model is generated in the setups of Fig. 3(a) and Fig. 4(a).

B. Perfect channel knowledge at source and receiver

Assume \mathbf{H}_a is perfectly known at both sides and let $\mathbf{H}_a = \mathbf{U}_a \Lambda_a \mathbf{V}_a^H$ be its singular value decomposition. The capacity in (55) is achieved by a circularly-symmetric, complex-Gaussian angular input $\mathbf{x}_a = \mathbf{V}_a \mathbf{P}_a^{1/2} \mathbf{s}_a$ where $\mathbf{s}_a \in \mathbb{C}^{n_s}$ is an i.i.d. circularly-symmetric complex-Gaussian vector with unit variance and $\mathbf{P}_a \in \mathbb{C}^{n_s \times n_s}$ is diagonal with entries given by the optimal powers. These are computed via the waterfilling algorithm (e.g., [25], [34]). Hence, \mathbf{x}_a has covariance matrix $\mathbf{Q}_a = \mathbf{V}_a \mathbf{P}_a \mathbf{V}_a^H$ and the ergodic capacity is

$$C = \sum_{i=1}^{\text{rank}(\mathbf{H}_a)} \log_2 (\mu \lambda_i(\mathbf{H}_a))^+ \quad (59)$$

where μ satisfies the constraint $\text{snr} = \sum_{i=1}^{\text{rank}(\mathbf{H}_a)} (\mu - 1/\lambda_i(\mathbf{H}_a))^+$. Fig. 8 plots (59) as a function of snr in dB. As snr grows large, an increasing number of communications modes is activated. In the large SNR regime, the capacity scales linearly in $\log_2(\text{snr})$ with slope given by the number of DoF in (49). Compared to i.i.d. Rayleigh fading and Clarke's model, the spatial correlation reduces the slope and introduces a negative shift in the capacity [24].

C. Statical knowledge of the channel at the source

The key message from the analysis in Section IV is that knowledge of the strength of coupling coefficients is needed to have full statistical knowledge of \mathbf{H}_a in (48). A possible way to obtain this information is sketched in Section IV-D. Suppose now that this knowledge is perfectly available at

the transmitter. Since \mathbf{H}_a has independent entries whose marginal distributions are symmetric with respect to zero, the optimal angular covariance matrix is diagonal, i.e., $\mathbf{Q}_a = \mathbf{P}_a$ [15, Th. 1]. The optimal \mathbf{x}_a is $\mathbf{x}_a = \mathbf{P}_a^{1/2} \mathbf{s}_a$ where the information-bearing vector $\mathbf{s}_a \in \mathbb{C}^{n_s}$ is an i.i.d. circularly-symmetric complex-Gaussian vector with unit variance. Hence, the capacity-achieving transmission strategy is to send statistically-independent streams of information angularly. Unlike the angular domain, in the spatial domain we have statistically correlated input symbols specified by the correlation matrix $\mathbf{Q} = \Phi_s \mathbf{Q}_a \Phi_s^H \in \mathbb{C}^{N_s \times N_s}$.

VI. CONCLUSIONS

We introduced a novel Fourier plane-wave stochastic channel model that is mathematically tractable and is consistent with the physics of wave propagation. The developed model is valid in the near-field and fully captures the essence of electromagnetic propagation under any scattering condition. It is especially for, but not limited to, conducting research on future wireless systems with large (compared to the wavelength) and dense antenna arrays. Our hope is to excite the interest of the wireless research community toward the need of physics-inspired channel models that may push further the limits of MIMO communications. Possible extension to the proposed Fourier plane-wave channel model may include mutual coupling effects between adjacent antenna elements (e.g., [35], [36]) and polarized antenna arrays [37], [38]. Real-world measurements are also needed to support the developed theory and correctly extract the model parameters for practical propagation scenarios.

APPENDIX

We aim to provide a discrete approximation of the Fourier plane-wave representation in (4) for a channel observed over a large spatial region of finite extent, as specified in Assumption 1. To this end, we follow the same approach exemplified in [3, App. IV.A] for a 1D time-domain random process and partition the integration region $\mathcal{D} \times \mathcal{D}$ of the 6D spatial random channel $h(\mathbf{r}, \mathbf{s})$ uniformly with angular sets $\mathcal{S}_s(m_x, m_y)$ and $\mathcal{S}_r(\ell_x, \ell_y)$ (see [3, Eq. (61)]):

$$\sum_{(\ell_x, \ell_y)} \sum_{(m_x, m_y)} \iiint_{\mathcal{S}_s(m_x, m_y) \times \mathcal{S}_r(\ell_x, \ell_y)} S^{1/2}(k_x, k_y, \kappa_x, \kappa_y) W(k_x, k_y, \kappa_x, \kappa_y) a_r(\mathbf{k}, \mathbf{r}) a_s(\boldsymbol{\kappa}, \mathbf{s}) \frac{dk_x dk_y}{2\pi} \frac{d\kappa_x d\kappa_y}{2\pi}. \quad (60)$$

where we substituted the angular response formula in (10) and $\mathcal{S}_s(m_x, m_y)$ and $\mathcal{S}_r(\ell_x, \ell_y)$ are given by (22) and (23), respectively. The application of the first mean-value theorem over each

partition yields the approximated Fourier series expansion in (19) where each random coefficient $H_a(\ell_x, \ell_y, m_x, m_y)$ with $(m_x, m_y) \in \mathcal{E}_s$ and $(\ell_x, \ell_y) \in \mathcal{E}_r$ is given by

$$\frac{1}{(2\pi)^2} \iiint_{\mathcal{S}_s(m_x, m_y) \times \mathcal{S}_r(\ell_x, \ell_y)} S^{1/2}(k_x, k_y, \kappa_x, \kappa_y) W(k_x, k_y, \kappa_x, \kappa_y) dk_x dk_y d\kappa_x d\kappa_y \quad (61)$$

which is obtained by projecting a 4D white noise complex-Gaussian field $W(k_x, k_y, \kappa_x, \kappa_y)$ over a set of orthonormal functions (see [3, Eq. (63)]). Hence, they are statistically-independent each other and distributed as circularly-symmetric, complex-Gaussian random variables [25]. The variances $\sigma^2(\ell_x, \ell_y, m_x, m_y)$ of the corresponding Fourier coefficients are obtained by computing the average power along each coordinate function as given by (21).

Next we derive a numerical generation procedure for computing the variances under arbitrary non-isotropic scattering conditions. Unlike [3, App. IV.C], where we were able to compute a closed form expression for the variances under isotropic scattering, here we resort to a general numerical procedure as solving (21) for every possible propagation conditions is pointless. Each variance $\sigma^2(\ell_x, \ell_y, m_x, m_y)$ is thus obtained by substituting (11) into (21):

$$\iiint_{\mathcal{S}_s(m_x, m_y) \times \mathcal{S}_r(\ell_x, \ell_y)} \mathbb{1}_{\mathcal{D}}(k_x, k_y) \mathbb{1}_{\mathcal{D}}(\kappa_x, \kappa_y) \frac{A^2(k_x, k_y, \kappa_x, \kappa_y)}{\gamma(k_x, k_y) \gamma(\kappa_x, \kappa_y)} dk_x dk_y d\kappa_x d\kappa_y \quad (62)$$

where $\mathbb{1}_{\mathcal{D}}(\cdot)$ accounts for the circularly-bandlimited support of the channel and the proportionality constants are embedded into the spectral factor $A^2(k_x, k_y, \kappa_x, \kappa_y)$ to meet the unit average power constraint $P_h = 1$. We focus on the receiver as the source follows similarly. The normalization of the wavevector coordinates (k_x, k_y, γ) to the wavenumber κ yields $(\hat{k}_x, \hat{k}_y, \hat{\gamma}) = (k_x, k_y, \gamma)/\kappa$ with

$$\hat{\gamma}(\hat{k}_x, \hat{k}_y) = \sqrt{1 - \hat{k}_x^2 - \hat{k}_y^2}. \quad (63)$$

In applying the above transformation we notice that $\mathbb{1}_{\mathcal{D}}(k_x, k_y)$ implies that $\hat{\gamma}(\hat{k}_x, \hat{k}_y) \in [0, 1]$. The triplet $(\hat{k}_x, \hat{k}_y, \hat{\gamma})$ are the cosine directions that specify every receive $\hat{\mathbf{k}}$ propagation direction as they correspond to the projections $\hat{\mathbf{k}}$ to the Cartesian axes $(\hat{\mathbf{x}}, \hat{\mathbf{y}}, \hat{\mathbf{z}})$. Consequently, $\hat{\mathcal{S}}_r(\ell_x, \ell_y)$ is the normalized angular set defined as

$$\hat{\mathcal{S}}_r(\ell_x, \ell_y) = \left\{ \left[\frac{\lambda \ell_x}{L_{R,x}}, \frac{\lambda(\ell_x + 1)}{L_{R,x}} \right] \times \left[\frac{\lambda \ell_y}{L_{R,y}}, \frac{\lambda(\ell_y + 1)}{L_{R,y}} \right] \right\}. \quad (64)$$

The above change of integration variables at source and receiver into (62) yields

$$\iiint_{\hat{\mathcal{S}}_s(m_x, m_y) \times \hat{\mathcal{S}}_r(\ell_x, \ell_y)} \mathbb{1}_{\hat{\mathcal{D}}}(\hat{k}_x, \hat{k}_y) \mathbb{1}_{\hat{\mathcal{D}}}(\hat{\kappa}_x, \hat{\kappa}_y) \frac{A^2(\hat{k}_x, \hat{k}_y, \hat{\kappa}_x, \hat{\kappa}_y)}{\hat{\gamma}(\hat{k}_x, \hat{k}_y) \hat{\gamma}(\hat{\kappa}_x, \hat{\kappa}_y)} d\hat{k}_x d\hat{k}_y d\hat{\kappa}_x d\hat{\kappa}_y \quad (65)$$

where $\hat{\mathcal{D}}$ is a centered disk of radius 1. The integration region in (65) at the receiver is illustrated in Fig. 9 for the first wavenumber quadrant only, that is, $(\ell_x, \ell_y) \in \mathcal{E}_r$ such that $\ell_x, \ell_y > 0$. Due to

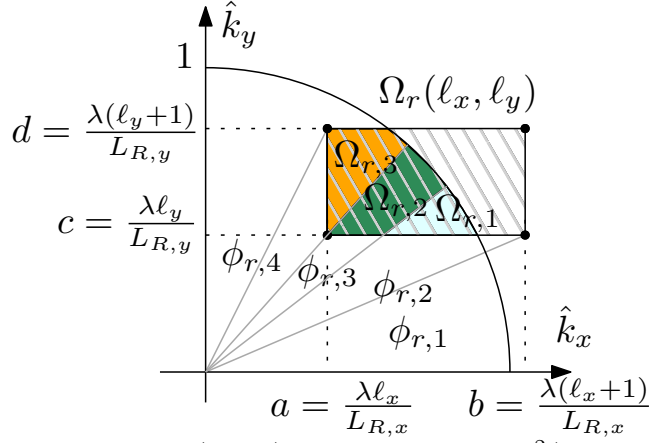


Fig. 9. Integration region $\Omega_r(\ell_x, \ell_y)$ of the variances $\sigma^2(\ell_x, \ell_y, m_x, m_y)$ in (68).

the rotational symmetry of the integrand we change integration variables in (65) to (normalized) polar wavenumber coordinates $(\hat{k}_x, \hat{k}_y) = (\hat{k}_r \cos \hat{k}_\phi, \hat{k}_r \sin \hat{k}_\phi)$ with $\hat{k}_r \in [0, 1]$ and $\hat{k}_\phi \in [0, 2\pi]$:

$$\iiint_{\hat{\mathcal{S}}_s(m_x, m_y) \times \hat{\mathcal{S}}_r(\ell_x, \ell_y)} \mathbb{1}_{[0,1]}(\hat{k}_r) \mathbb{1}_{[0,1]}(\hat{k}_r) \frac{A^2(\hat{k}_r, \hat{k}_\phi, \hat{\kappa}_r, \hat{\kappa}_\phi) \hat{k}_r \hat{\kappa}_r}{\sqrt{1 - \hat{k}_r^2} \sqrt{1 - \hat{\kappa}_r^2}} d\hat{k}_r d\hat{k}_\phi d\hat{\kappa}_r d\hat{\kappa}_\phi. \quad (66)$$

Polar wavenumber coordinates can be related to the standard spherical coordinates, i.e., elevation $(\theta_s, \theta_r) \in [0, \pi]$ and azimuth $(\phi_s, \phi_r) \in [0, 2\pi]$ angles. In doing so, the terms at the denominator of (66) disappear as they are embedded into the Jacobian of this transformation. In particular, the map between the two representation is given by $\hat{k}_x = \sin \theta_r \cos \phi_r$ and $\hat{k}_y = \sin \theta_r \sin \phi_r$ which substituted into (63) yields $\hat{\gamma}(\hat{k}_x, \hat{k}_y) = \cos \theta_r \in [0, 1]$. Notice that the circularly-bandlimited constraint implies that $\theta_r \in [0, \pi/2]$. In other words, we consider propagation directions $\hat{\mathbf{k}}$ defined over the unit upper hemisphere $\mathcal{S}_+ = \{(\theta_r, \phi_r) : \theta_r \in [0, \pi/2], \phi_r \in [0, 2\pi]\}$.⁴ The polar wavenumber coordinates follow directly as $\hat{k}_r = \sin \theta_r$ and $\hat{k}_\phi = \phi_r$ with Jacobian given by $|\partial(\hat{k}_r, \hat{k}_\phi)/\partial(\theta_r, \phi_r)| = \cos \theta_r$. Applying the above transformation at source and receiver into (66) yields

$$\iiint_{\hat{\mathcal{S}}_s(m_x, m_y) \times \hat{\mathcal{S}}_r(\ell_x, \ell_y)} \mathbb{1}_{[0, \pi/2]}(\theta_r) \mathbb{1}_{[0, \pi/2]}(\theta_s) A^2(\theta_r, \phi_r, \theta_s, \phi_s) d\Omega_s d\Omega_r \quad (67)$$

where $d\Omega_r = \sin \theta_r d\theta_r d\phi_r$ and $d\Omega_s = \sin \theta_s d\theta_s d\phi_s$ are the differential element of solid angles pointed by $\hat{\kappa}$ and $\hat{\mathbf{k}}$. The above formula can be compactly rewritten as

$$\sigma^2(\ell_x, \ell_y, m_x, m_y) = \iiint_{\Omega_s(m_x, m_y) \times \Omega_r(\ell_x, \ell_y)} A^2(\theta_r, \phi_r, \theta_s, \phi_s) d\Omega_s d\Omega_r \quad (68)$$

where we defined the integration region, e.g., at the receiver, as

$$\Omega_r(\ell_x, \ell_y) = \hat{\mathcal{S}}_r(\ell_x, \ell_y) \cap \{\theta_r \in [0, \pi/2], \phi \in [0, 2\pi]\}. \quad (69)$$

⁴The unit lower hemisphere \mathcal{S}_- follows similarly but replacing $-\hat{\gamma}(\hat{k}_x, \hat{k}_y)$ with $\hat{\gamma}(\hat{k}_x, \hat{k}_y)$, which leads to $\theta_r \in (\pi/2, \pi]$. Physically, this corresponds to a propagation scenario with backscattering and is not considered in this paper [21, Sec. VII].

Next, we properly define the integration region $\Omega_r(\ell_x, \ell_y)$ in (69) for $(\ell_x, \ell_y) \in \mathcal{E}_r$ as a function of the spherical angles (θ_r, ϕ_r) . This is specified in terms of the auxiliary quantities $a = \lambda \ell_x / L_{R_x}$, $b = \lambda(\ell_x + 1) / L_{R_x}$, $c = \lambda \ell_y / L_{R_y}$, and $d = \lambda(\ell_y + 1) / L_{R_y}$, which are the cosine directions evaluated in correspondence of the four vertices of $\hat{\mathcal{S}}_r(\ell_x, \ell_y)$ in (64). As shown in Fig. 9, these four vertices angularly divide the integration region $\Omega_r(\ell_x, \ell_y)$ into three subregions: $\phi_r \in [\phi_{r,1}, \phi_{r,2}]$, $\phi_r \in [\phi_{r,2}, \phi_{r,3}]$, and $\phi_r \in [\phi_{r,3}, \phi_{r,4}]$, which are limited by the azimuth angles $\phi_{r,1} < \phi_{r,2} < \phi_{r,3} < \phi_{r,4}$. Hence, (68) can be rewritten as

$$\sigma^2(\ell_x, \ell_y, m_x, m_y) = \sum_{i=1}^3 \sum_{j=1}^3 \iiint_{\Omega_{r,i}(\ell_x, \ell_y) \times \Omega_{s,j}(m_x, m_y)} A^2(\theta_r, \phi_r, \theta_s, \phi_s) d\Omega_s d\Omega_r \quad (70)$$

where $\Omega_{r,i}(\ell_x, \ell_y) = \{(\theta_r, \phi_r) : \theta_r \in [\theta_{r,\min}(\phi_r), \theta_{r,\max}(\phi_r)], \phi_r \in [\phi_{r,i}, \phi_{r,i+1}]\}$. The above angular sets for $(\ell_x, \ell_y) \in \mathcal{E}_r$ are specified next for each one of the four orthants separately.

a) *First orthant* $\phi_r \in [0, \pi/2]$: The first orthant corresponds to $(\ell_x, \ell_y) \in \mathcal{E}_r$ such that $\ell_x \geq 0$ and $\ell_y \geq 0$. For every such (ℓ_x, ℓ_y) we have that $\phi_{r,1} = \arctan(c/b)$, $\phi_{r,2} = \min(\arctan(c/a), \arctan(d/b))$, $\phi_{r,3} = \max(\arctan(c/a), \arctan(d/b))$, and $\phi_{r,4} = \arctan(d/a)$. The integration θ_r interval parametrized by ϕ_r is:

$$\begin{aligned} \Omega_{r,1}(\ell_x, \ell_y): \theta_{r,\min}(\phi_r) &= \arcsin(\min(1, c / \sin \phi_r)) \text{ and } \theta_{r,\max}(\phi_r) = \arcsin(\min(1, b / \cos \phi_r)); \\ \Omega_{r,2}(\ell_x, \ell_y), \ell_x \geq \ell_y: \theta_{r,\min}(\phi_r) &= \arcsin(\min(1, a / \cos \phi_r)) \text{ and } \theta_{r,\max}(\phi_r) = \arcsin(\min(1, b / \cos \phi_r)). \\ \Omega_{r,2}(\ell_x, \ell_y), \ell_x < \ell_y: \theta_{r,\min}(\phi_r) &= \arcsin(\min(1, c / \sin \phi_r)) \text{ and } \theta_{r,\max}(\phi_r) = \arcsin(\min(1, d / \sin \phi_r)). \\ \Omega_{r,3}(\ell_x, \ell_y): \theta_{r,\min}(\phi_r) &= \arcsin(\min(1, a / \cos \phi_r)) \text{ and } \theta_{r,\max}(\phi_r) = \arcsin(\min(1, d / \sin \phi_r)). \end{aligned}$$

b) *Second orthant* $\phi_r \in [\pi/2, \pi]$: The second orthant corresponds to $(\ell_x, \ell_y) \in \mathcal{E}_r$ such that $\ell_x < 0$ and $\ell_y \geq 0$. For every such (ℓ_x, ℓ_y) we have that $\phi_{r,1} = \pi - \arctan(d/|b|)$, $\phi_{r,2} = \pi - \max(\arctan(c/|b|), \arctan(d/|a|))$, $\phi_{r,3} = \pi - \min(\arctan(c/|b|), \arctan(d/|a|))$, and $\phi_{r,4} = \pi - \arctan(c/|a|)$. The integration θ_r interval parametrized by ϕ_r is:

$$\begin{aligned} \Omega_{r,1}(\ell_x, \ell_y): \theta_{r,\min}(\phi_r) &= \arcsin(\min(1, |b| / \cos(\pi - \phi_r))) \text{ and } \theta_{r,\max}(\phi_r) = \arcsin(\min(1, d / \sin(\pi - \phi_r))). \\ \Omega_{r,2}(\ell_x, \ell_y), |\ell_x| > \ell_y: \theta_{r,\min}(\phi_r) &= \arcsin(\min(1, |b| / \cos(\pi - \phi_r))) \\ \text{and } \theta_{r,\max}(\phi_r) &= \arcsin(\min(1, |a| / \cos(\pi - \phi_r))). \end{aligned}$$

$$\begin{aligned} \Omega_{r,2}(\ell_x, \ell_y), |\ell_x| \leq \ell_y: \theta_{r,\min}(\phi_r) &= \arcsin(\min(1, c / \sin(\pi - \phi_r))) \\ \text{and } \theta_{r,\max}(\phi_r) &= \arcsin(\min(1, d / \sin(\pi - \phi_r))). \end{aligned}$$

$$\Omega_{r,3}(\ell_x, \ell_y): \theta_{r,\min}(\phi_r) = \arcsin(\min(1, c / \sin(\pi - \phi_r))) \text{ and } \theta_{r,\max}(\phi_r) = \arcsin(\min(1, |a| / \cos(\pi - \phi_r))).$$

c) *Third orthant* $\phi_r \in [\pi, 3\pi/2]$: The third orthant corresponds to $(\ell_x, \ell_y) \in \mathcal{E}_r$ such that $\ell_x < 0$ and $\ell_y < 0$. For every such (ℓ_x, ℓ_y) we have that $\phi_{r,1} = \pi + \arctan(|d|/|a|)$, $\phi_{r,2} =$

$\pi + \min(\arctan(|d|/|b|), \arctan(|c|/|a|))$, $\phi_{r,3} = \pi + \max(\arctan(|d|/|b|), \arctan(|c|/|a|))$, and $\phi_{r,4} = \pi + \arctan(|c|/|b|)$. The integration θ_r interval parametrized by ϕ_r is:

$\Omega_{r,1}(\ell_x, \ell_y)$: $\theta_{r,\min}(\phi_r) = \arcsin(\min(1, |d|/\sin(\phi_r - \pi)))$ and $\theta_{r,\max}(\phi_r) = \arcsin(\min(1, |a|/\cos(\phi_r - \pi)))$.

$\Omega_{r,2}(\ell_x, \ell_y)$, $|\ell_x| \geq |\ell_y|$: $\theta_{r,\min}(\phi_r) = \arcsin(\min(1, |b|/\cos(\phi_r - \pi)))$

and $\theta_{r,\max}(\phi_r) = \arcsin(\min(1, |a|/\cos(\phi_r - \pi)))$.

$\Omega_{r,2}(\ell_x, \ell_y)$, $|\ell_x| < |\ell_y|$: $\theta_{r,\min}(\phi_r) = \arcsin(\min(1, |d|/\sin(\phi_r - \pi)))$

and $\theta_{r,\max}(\phi_r) = \arcsin(\min(1, |c|/\sin(\phi_r - \pi)))$.

$\Omega_{r,3}(\ell_x, \ell_y)$: $\theta_{r,\min}(\phi_r) = \arcsin(\min(1, |b|/\cos(\phi_r - \pi)))$ and $\theta_{r,\max}(\phi_r) = \arcsin(\min(1, |c|/\sin(\phi_r - \pi)))$.

d) *Fourth orthant* $\phi_r \in [3\pi/2, 2\pi]$: The fourth orthant corresponds to $(\ell_x, \ell_y) \in \mathcal{E}_r$ such that $\ell_x \geq 0$ and $\ell_y < 0$. For every such (ℓ_x, ℓ_y) we have that $\phi_{r,1} = 2\pi - \arctan(|c|/a)$, $\phi_{r,2} = 2\pi - \max(\arctan(|c|/b), \arctan(|d|/a))$, $\phi_{r,3} = 2\pi - \min(\arctan(|c|/b), \arctan(|d|/a))$, and $\phi_{r,4} = 2\pi - \arctan(|d|/b)$. The integration θ_r interval parametrized by ϕ_r is:

$\Omega_{r,1}(\ell_x, \ell_y)$: $\theta_{r,\min}(\phi_r) = \arcsin(\min(1, a/\cos(2\pi - \phi_r)))$ and $\theta_{r,\max}(\phi_r) = \arcsin(\min(1, |c|/\sin(2\pi - \phi_r)))$.

$\Omega_{r,2}(\ell_x, \ell_y)$, $\ell_x \geq |\ell_y|$: $\theta_{r,\min}(\phi_r) = \arcsin(\min(1, a/\cos(2\pi - \phi_r)))$

and $\theta_{r,\max}(\phi_r) = \arcsin(\min(1, b/\cos(2\pi - \phi_r)))$.

$\Omega_{r,2}(\ell_x, \ell_y)$, $\ell_x < |\ell_y|$: $\theta_{r,\min}(\phi_r) = \arcsin(\min(1, |d|/\sin(2\pi - \phi_r)))$

and $\theta_{r,\max}(\phi_r) = \arcsin(\min(1, |c|/\sin(2\pi - \phi_r)))$.

$\Omega_{r,3}(\ell_x, \ell_y)$: $\theta_{r,\min}(\phi_r) = \arcsin(\min(1, |d|/\sin(2\pi - \phi_r)))$ and $\theta_{r,\max}(\phi_r) = \arcsin(\min(1, b/\cos(2\pi - \phi_r)))$.

REFERENCES

- [1] A. Pizzo, T. L. Marzetta, and L. Sanguinetti, “Holographic MIMO Communications Under Spatially-Stationary Scattering,” *CoRR*, vol. abs/2012.07389, 2020. Online: <https://arxiv.org/abs/2012.07389>.
- [2] A. Pizzo, T. L. Marzetta, and L. Sanguinetti, “Degrees of Freedom of Holographic MIMO Channels,” in *2020 IEEE 21st Int. Workshop Signal Process. Adv. Wireless Commun. (SPAWC)*, 2020, pp. 1–5.
- [3] A. Pizzo, T. L. Marzetta, and L. Sanguinetti, “Spatially-Stationary Model for Holographic MIMO Small-Scale Fading,” *IEEE J. Sel. Areas Commun.*, vol. 38, no. 9, pp. 1964–1979, 2020.
- [4] D. Dardari and N. Decarli, “Holographic Communication using Intelligent Surfaces,” *CoRR*, vol. abs/2012.01315, 2020. Online: <https://arxiv.org/abs/2012.01315>.
- [5] S. Hu, F. Rusek, and O. Edfors, “Beyond Massive MIMO: The potential of data transmission with large intelligent surfaces,” *IEEE Trans. Signal Proc.*, vol. 66, no. 10, May 2018.
- [6] D. Dardari, “Communicating with large intelligent surfaces: Fundamental limits and models,” *IEEE Journal on Selected Areas in Communications*, vol. 38, no. 11, pp. 2526–2537, 2020.
- [7] Q. Wu and R. Zhang, “Intelligent Reflecting Surface Enhanced Wireless Network: Joint Active and Passive Beamforming Design,” in *2018 IEEE Global Communications Conference (GLOBECOM)*, 2018, pp. 1–6.

- [8] E. Basar, M. Di Renzo, J. De Rosny, M. Debbah, M. S. Alouini, and R. Zhang, “Wireless Communications Through Reconfigurable Intelligent Surfaces,” *IEEE Access*, vol. 7, pp. 116753–116773, 2019.
- [9] Y. Xing and T. S. Rappaport, “Propagation Measurements and Path Loss Models for sub-THz in Urban Microcells,” *CoRR*, vol. abs/2103.01151, 2021. Online: <https://arxiv.org/abs/2103.01151>.
- [10] T. K. Sarkar, Zhong Ji, Kyungjung Kim, A. Medouri, and M. Salazar-Palma, “A survey of various propagation models for mobile communication,” *IEEE Antennas and Propagation Magazine*, vol. 45, no. 3, pp. 51–82, 2003.
- [11] T. L. Marzetta, “Spatially-stationary propagating random field model for Massive MIMO small-scale fading,” in *2018 IEEE Int. Symposium Inf. Theory (ISIT)*, June 2018, pp. 391–395.
- [12] W. C. Chew, *Waves and Fields in Inhomogenous Media*, Wiley-IEEE Press, 1995.
- [13] A. S. Y. Poon, D. N. C. Tse, and R. W. Brodersen, “Impact of scattering on the capacity, diversity, and propagation range of multiple-antenna channels,” *IEEE Trans. Inf. Theory*, vol. 52, no. 3, March 2006.
- [14] A. M. Sayeed, “Deconstructing multiantenna fading channels,” *IEEE Trans. Signal Process.*, vol. 50, no. 10, 2002.
- [15] V. V. Veeravalli, Y. Liang, and A. M. Sayeed, “Correlated MIMO Wireless Channels: Capacity, Optimal Signaling, and Asymptotics,” *IEEE Trans. Inf. Theory*, vol. 51, no. 6, pp. 2058–2072, 2005.
- [16] A. S. Y. Poon, R. W. Brodersen, and D. N. C. Tse, “Degrees of freedom in multiple-antenna channels: a signal space approach,” *IEEE Trans. Inf. Theory*, vol. 51, no. 2, pp. 523–536, Feb 2005.
- [17] T. S. Pollock, T. D. Abhayapala, and R. A. Kennedy, “Spatial Limits to MIMO Capacity in General Scattering Environments,” in *7th International symposium on DSP Communication Systems (DSPCS03)*, 2003, vol. 1, pp. 49–54.
- [18] T. D. Abhayapala, T. S. Pollock, and R. A. Kennedy, “Spatial Decomposition of MIMO Wireless Channels,” in *Seventh International Symposium on Signal Processing and Its Applications, 2003. Proceedings.*, 2003, vol. 1, pp. 309–312.
- [19] E. Björnson, J. Hoydis, and L. Sanguinetti, *Massive MIMO Networks: Spectral, Energy, and Hardware Efficiency*, vol. 11, Foundations and Trends in Signal Processing, 2017.
- [20] T. B. Hansen T. L. Marzetta, E. G. Larsson, “Massive MIMO and Beyond,” in *Information Theoretic Perspectives on 5G Systems and Beyond*, S. Shamai I. Maric, O. Simeone, Ed. Cambridge University Press, Cambridge, 2020.
- [21] A. Pizzo, L. Sanguinetti, and T. L. Marzetta, “Spatial Characterization of Electromagnetic Random Channels,” *CoRR*, vol. abs/2103.15666, 2021. Online: <https://arxiv.org/abs/2103.15666>.
- [22] H. L. Van Trees, *Detection Estimation and Modulation Theory, Part I*, Wiley, 1968.
- [23] D. Tse and P. Viswanath, *Fundamentals of Wireless Communication*, Cambridge University Press, 2005.
- [24] R. W. Heath Jr. and A. Lozano, *Foundations of MIMO Communication*, Cambridge University Press, 2018.
- [25] R. G. Gallager, *Principles of Digital Communication*, Cambridge University Press, 2008.
- [26] D. A. B. Miller, “Communicating with waves between volumes: evaluating orthogonal spatial channels and limits on coupling strengths,” *Appl. Opt.*, vol. 39, no. 11, pp. 1681–1699, Apr 2000.
- [27] M. Franceschetti, *Wave Theory of Information*, Cambridge University Press, 2017.
- [28] A. M. Tulino, A. Lozano, and S. Verdu, “Impact of antenna correlation on the capacity of multiantenna channels,” *IEEE Trans. Inf. Theory*, vol. 51, no. 7, pp. 2491–2509, 2005.
- [29] M. Franceschetti, “On Landau’s eigenvalue theorem and information cut-sets,” *IEEE Trans. Inf. Theory*, vol. 61, no. 9, Sept 2015.
- [30] W. Weichselberger, M. Herdin, H. Ozcelik, and E. Bonek, “A stochastic MIMO channel model with joint correlation of both link ends,” *IEEE Trans. Wireless Commun.*, vol. 5, no. 1, pp. 90–100, 2006.
- [31] E. Björnson and L. Sanguinetti, “Rayleigh Fading Modeling and Channel Hardening for Reconfigurable Intelligent Surfaces,” *CoRR*, vol. abs/2009.04723, 2020. Online: <https://arxiv.org/abs/2009.04723>.

- [32] A. F. Molisch and X. Zhang, "FFT-based Hybrid Antenna Selection Schemes for Spatially Correlated MIMO Channels," *IEEE Commun. Letters*, vol. 8, no. 1, pp. 36–38, 2004.
- [33] Y. Zeng and R. Zhang, "Millimeter wave MIMO with lens antenna array: A new path division multiplexing paradigm," *IEEE Transactions on Communications*, vol. 64, no. 4, pp. 1557–1571, 2016.
- [34] E. Telatar, "Capacity of Multi-antenna Gaussian Channels," *European Trans. Telecommun.*, vol. 10, no. 6.
- [35] I. Gupta and A. Ksienki, "Effect of mutual coupling on the performance of adaptive arrays," *IEEE Transactions on Antennas and Propagation*, vol. 31, no. 5, pp. 785–791, 1983.
- [36] R. Janaswamy, "Effect of element mutual coupling on the capacity of fixed length linear arrays," *IEEE Antennas and Wireless Propagation Letters*, vol. 1, pp. 157–160, 2002.
- [37] T. L. Marzetta, "Fundamental Limitations on the Capacity of Wireless Links that use Polarimetric Antenna Arrays," in *Proceedings IEEE International Symposium on Information Theory*, 2002, pp. 51–.
- [38] T. L. Marzetta, "BLAST Arrays of Polarimetric Antennas," ITD-01-41984K, Nokia Proprietary, 10 05 2001.